

Analysis of Rayleigh–Plesset dynamics for sonoluminescing bubbles

By

**SASCHA HILGENFELDT¹, MICHAEL P. BRENNER²,
SIEGFRIED GROSSMANN¹, AND DETLEF LOHSE¹**

¹ Fachbereich Physik der Universität Marburg, Renthof 6, 35032 Marburg, Germany

² Department of Mathematics, MIT, Cambridge, MA 02139

(Received 22 February 1997 and in revised form 21 January 1998)

Recent work on single bubble sonoluminescence (SBSL) has shown that many features of this phenomenon, especially the dependence of SBSL intensity and stability on experimental parameters, can be explained within a *hydrodynamic approach*. More specifically, many important properties can already be derived from an analysis of *bubble wall dynamics*. This dynamics is conveniently described by the Rayleigh–Plesset (RP) equation. In this work we derive analytical approximations for RP dynamics and subsequent analytical laws for parameter dependences. These results include (i) an expression for the onset threshold of SL, (ii) an analytical explanation of the transition from diffusively unstable to stable equilibria for the bubble ambient radius (unstable and stable sonoluminescence), and (iii) a detailed understanding of the resonance structure of the RP equation. It is found that the threshold for SL emission is shifted to larger bubble radii and larger driving pressures if surface tension is enlarged, whereas even a considerable change in liquid viscosity leaves this threshold virtually unaltered. As an enhanced viscosity stabilizes the bubbles against surface oscillations, we conclude that the ideal liquid for violently collapsing, surface stable SL bubbles should have small surface tension and large viscosity, although too large viscosity ($\eta_l \gtrsim 40\eta_{\text{water}}$) will again preclude collapses.

1. Introduction

1.1. Sonoluminescence

The analysis of the dynamics of a small bubble or cavity in a fluid dates back to the work of Lord Rayleigh (1917) at the beginning of this century. A large number of publications followed in subsequent decades, including the studies of oscillating bubbles by Plesset (1949, 1954), Eller & Crum (1970), Flynn (1975a, 1975b), Lauterborn (1976), Prosperetti (1977), Plesset & Prosperetti (1977), and others. In recent years, a renascence of bubble dynamics has occurred initiated by the discovery of single bubble sonoluminescence (SBSL) by Gaitan (1990), see also Gaitan *et al.* (1992).

SBSL is an intriguing phenomenon: A single gas bubble of only a few μm size, levitated in water by an acoustic standing wave, emits light pulses so intense as to be visible to the naked eye. The standing ultrasound wave of the driving keeps the bubble in position at a pressure antinode and, at the same time, drives its oscillations. The experiments of Puttermann's group (Barber & Puttermann 1991; Barber *et al.* (1994, 1995); Hiller *et al.* 1994; Löfstedt, Barber & Puttermann 1993; Löfstedt *et al.* 1995; Weninger, Puttermann & Barber 1996) and others have revealed a multitude of interesting facts about SBSL: the width of the light pulse is small (Barber & Puttermann 1991 give 50 ps as upper threshold, Moran *et al.* 1995 10 ps – recent measurements by Gompf *et al.* 1997 report 100-300 ps , depending on the forcing pressure and gas concentration in the liquid), the spectrum shows no features such as lines (Hiller, Puttermann & Barber 1992; Matula *et al.* 1995). While the exact mechanism of light emission is still an open issue, almost all suggested theories – see e.g. Löfstedt *et al.* (1993), Hiller *et al.* (1992), Flint & Suslick (1989), Wu & Roberts (1993), Frommhold & Atchley (1994), Moss *et al.* (1994), Bernstein & Zakin (1995), Moss, Clarke & Young (1997) – agree that temperatures of at least 10^4 - 10^5 K are reached during bubble collapse. This, together with the light intensity, clearly shows that SBSL relies on an extraordinarily powerful energy focusing process.

In our previous publications Brenner, Lohse & Dupont (1995), Brenner *et al.* (1996a, 1996b), Hilgenfeldt, Lohse & Brenner (1996), Brenner, Hilgenfeldt & Lohse (1996), Lohse *et al.* (1997), and Lohse & Hilgenfeldt (1997) we calculated phase diagrams for bubbles and have focused on the identification of parameter regimes where SBSL occurs. As a scan of the whole multi-dimensional parameter space is by far too expensive for full numerical simulations of the underlying fundamental equations (i.e., Navier–Stokes and advection-diffusion PDEs), it is necessary to introduce approximations. The necessary conditions for SL to occur could be calculated from the dynamics $R(t)$ of the bubble wall, which is – apart from a tiny interval around the bubble collapse – very well described by the Rayleigh–Plesset (RP) equation. We call this approach the *RP-SL bubble approach*.

The key parameters in an SL experiment are the ambient bubble radius R_0 (radius under normal conditions of $1.013 \times 10^5 \text{ Pa} = 1 \text{ atm}$ and 20°C), the driving pressure amplitude P_a , and the gas concentration in the water surrounding the bubble p_∞/P_0 , measured by its partial pressure divided by the ambient pressure. Note that R_0 is not at the experimenter's disposal, but adjusts itself by gas diffusion on a slow time scale of seconds. Its size can, however, be measured in experiment, e.g., by Mie scattering techniques as in Barber *et al.* (1995) or by direct microscopic imaging, see Tian, Ketterling & Apfel (1996), Holt & Gaitan (1996). On time scales much smaller than those of diffusive processes, e.g. for one period of driving, R_0 may be regarded as a constant to high accuracy.

In Hilgenfeldt *et al.* (1996) we found that the $P_a/P_0 - p_\infty/P_0$ state space is divided into regions where (diffusively) *stable SL*, *unstable SL* or *no SL* are to be expected, in excellent

agreement with experimental findings. These results will now be briefly presented in the following subsection.

1.2. Stability requirements

Stable sonoluminescence is characterized by light emission in each period of driving at precisely the same oscillation phase and precisely the same brightness for millions (and sometimes billions) of cycles. We found that it occurs in a tiny section of the whole parameter space only, and that the calculated domain agrees very well with experimental findings, cf. Hilgenfeldt *et al.* (1996), Lohse *et al.* (1997). Its boundaries are set by certain dynamical and stability conditions imposed upon the oscillating bubble (Brenner *et al.* 1995, Brenner *et al.* 1996a, Hilgenfeldt *et al.* 1996): (i) The bubble wall velocity during collapse must reach the speed of sound in the gas c_g to ensure sufficient energy transfer from the liquid to the gas. (ii) The bubble must be stable towards non-spherical oscillations of its surface which lead to fragmentation. Bubble fragments have meanwhile been experimentally observed by J. Holzfuss (private communication, 1997). (iii) The bubble must be stable towards diffusive processes, i.e., it must not dissolve or grow by rectified diffusion; diffusively growing bubbles show *unstable SL*. A further requirement of (iv) chemical stability becomes important when the bubble contains molecular gases which are able to dissociate and recombine with liquid molecules (Brenner *et al.* 1996, Lohse *et al.* 1997). E.g., the differences in the parameter regimes of SL in air bubbles vs. SL in noble gas bubbles can consistently be accounted for by dissociation of N_2 and O_2 in an air bubble; these molecular constituents of air are burned, leaving only inert gases in the bubble (the experimental work of Holt & Gaitan 1996 supports this model). We therefore restrict ourselves for simplicity to the case of a bubble filled with argon. An extension to reactive gas mixtures as analysed in Lohse *et al.* (1997) is straightforward. Also, we specify the liquid in which the bubble oscillates to be water, as in most SBSL experiments.

Figure 1 illustrates how the conditions (i)–(iii) determine domain boundaries in the P_a – R_0 state space. Criterion (i) means that the Mach number with respect to c_g is larger than 1, i.e.,

$$|M_g| = \frac{|\dot{R}|}{c_g} \gtrsim 1, \quad (1.1)$$

and it is fulfilled for bubbles with large enough ambient radii R_0 and at large enough forcing amplitude P_a , i.e., right of the dashed line in figure 1. The shape stability condition (ii) – see Plesset (1954), Birkhoff (1954), Eller & Crum (1970), Strube (1971), Prosperetti (1977), Brenner *et al.* (1995) or Hilgenfeldt *et al.* (1996) for detailed studies –, on the other hand, limits the parameter domain in which bubbles can stably oscillate to small $R_0 \lesssim 4 - 5 \mu m$, within our boundary layer approximation. As the RP SL approach neglects effects of thermal conduction, which has a damping influence on surface oscillations, this upper limit on R_0 may be somewhat higher in reality. Holt & Gaitan's (1996) experimental results seem to give a threshold around $7 \mu m$. (i) and (ii) together determine the shaded area of potentially sonoluminescing bubbles in figure 1.

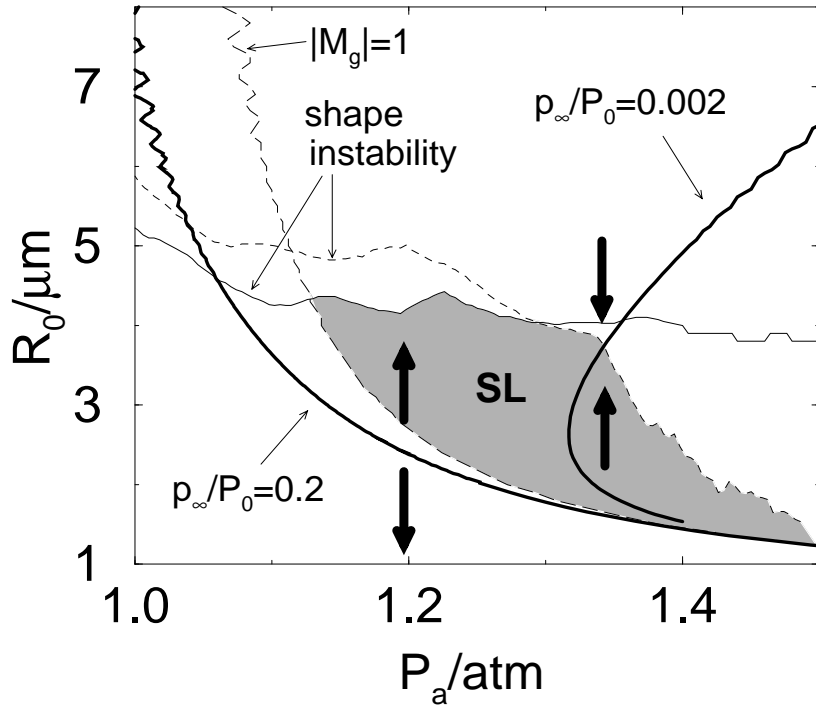


FIGURE 1. Stability conditions for a bubble in P_a - R_0 parameter space. Bubbles above the line $|M_g| = 1$ fulfill the energy focusing condition (1.1). Bubbles below the shape instability lines are stable towards non-spherical surface oscillations. The solid line represents the (long time scale) parametric instability, the dashed line short time scale shape instabilities, for details see Hilgenfeldt *et al.* (1996). Bubbles on the thick lines are in diffusive equilibrium for $p_\infty/P_0 = 0.2, 0.002$, respectively. Thick arrows indicate regions of bubble growth and shrinking by diffusive processes.

The actual position of a stable SL bubble in P_a - R_0 parameter space is determined by condition (iii) for stable diffusive equilibria of the gas inside the bubble and the dissolved gas in the liquid (thick lines in figure 1). These equilibrium lines show negative slope whenever the equilibria are unstable, i.e., bubbles below the line shrink and dissolve, bubbles above the line grow. At large gas concentrations in the liquid (e.g. $p_\infty/P_0 \sim 0.2$, left curve), only unstable equilibria are possible in the parameter range of interest. Tiny ratios $p_\infty/P_0 \sim 0.002$ (right curve) are necessary for diffusive stability (i.e., the fluid must be strongly degassed). The positive slope of the upper branch of the curve characterizes these bubbles as stable. The computation of diffusive equilibria is explained in § 2.2.

1.3. Summary of results of the present work

Having identified the parameter regions for SBSL through numerically solving the RP equation, the question arises if one can understand the shape and size of these regions

analytically, i.e., by analysing the bubble dynamics equations. In principle, all of the conditions that determine the occurrence of stable/unstable/no SL depend only on properties of bubble dynamics. Therefore, we set out in this work to derive analytical approximations for RP dynamics and subsequently find scaling laws or approximate analytical expressions for our numerical curves presented above, in order to give a clearer insight into the role of different physical processes governing the dynamical equations. Moreover, more practical reasons make analytical expressions highly desirable, as the multi-dimensional parameter space of SBSL experiments cannot be scanned in detail just by numerical solution of the RP equation. Our analytical efforts strongly build on previous work, most notably that of Löfstedt *et al.* (1993). We present the most important results in this subsection, written such that experimental parameters can be directly inserted to yield numerical values. Here we have used fixed $\omega = 2\pi \times 26.5 \text{ kHz}$ and $P_0 = 1 \text{ atm}$. More detailed results and the complete derivations for general ω, P_0 will be given in the corresponding Sections. All the presented approximations naturally have limited parameter regimes of validity, which include the region of sonoluminescing bubbles in all cases.

We will demonstrate in § 2 that, in order to understand the location of diffusive equilibria, it is sufficient to analyse the parameter dependence of the ratio of the maximum bubble radius to its ambient radius (R_{\max}/R_0), see Löfstedt *et al.* (1993). We show in § 3 that two clearly distinct kinds of bubble dynamical behaviour exist depending on P_a and R_0 : *weakly oscillating* and *strongly collapsing* bubbles. The transition between these two states is rather abrupt and occurs for given P_a at an ambient radius

$$R_0^{tr} = \frac{4}{9}\sqrt{3}\frac{\sigma}{P_a - P_0} \approx \frac{0.562 \mu\text{m}}{P_a/P_0 - 1}. \quad (1.2)$$

This transition is controlled by the surface tension σ , i.e., strong collapses are easier to achieve for small σ .

In § 4, we derive analytical approximations to RP dynamics for all phases of the oscillation cycle of a strongly collapsing bubble. We find that in this regime the bubble essentially collapses like an empty cavity (see Rayleigh (1917)) according to

$$R(t) \approx 14.3 \mu\text{m} \cdot \left(\frac{R_{\max}}{\mu\text{m}}\right)^{3/5} \left(\frac{t^* - t}{T}\right)^{2/5}, \quad (1.3)$$

with the time of maximum bubble compression t^* and the driving period $T = 2\pi/\omega$.

Following the collapse, a series of characteristic afterbounces of the bubble radius occurs. We show in § 4.3 that they are the cause for the wiggly structure of the diffusive equilibrium curves and the $|M_g| = 1$ line in figure 1. The location of the wiggles can be understood as a parametric resonance phenomenon. A Mathieu approximation yields the ambient radius of the k^{th} wiggle as

$$R_0^{(k)} \approx 37.0 \mu\text{m} \cdot \frac{q^{5/3}}{\sqrt{q^{5/3} - 1}} \frac{1}{k} + 0.487 \mu\text{m} \cdot \left(\frac{q^{5/3} - 2q + 1}{q^{5/3} - 1} + 2\frac{2 - q^{2/3}}{q^{2/3}}\right) \quad (1.4)$$

with the abbreviation $q = (1 + P_a/P_0)$.

Section 4.4 deals with the bubble expansion. In the regime of strong bubble collapses,

an approximate result for the dependence of the maximum radius on P_a and R_0 is

$$\frac{R_{max}}{\mu m} \approx 67.2 + 0.112 \left(\frac{R_0}{\mu m} \right)^2 + 99.5(P_a/P_0 - \pi/2). \quad (1.5)$$

With R_{max} , the location of diffusive equilibria in (P_a, R_0) parameter space can be calculated.

A closer discussion of the role of surface tension and viscosity of the liquid η_l is presented in § 5. In particular, the viscosity of water is so small that it has no significant influence on bubble dynamics. Oscillations are only viscosity-dominated if

$$\eta_l^c \gtrsim \left(1 + \frac{0.487 \mu m}{R_0} \right) \cdot 8.72 \left(\frac{R_0}{\mu m} \right) \eta_{water}, \quad (1.6)$$

which corresponds to $\eta_l \gtrsim 40\eta_{water}$ for typical R_0 .

Note that these equations are *not* fit formulas, but are analytically *derived* from the RP dynamics. They are all verified by comparison to full numerical solutions in the appropriate domains of validity. With these formulas, we are able to understand most of the parameter dependences of SL analytically. Section 6 presents conclusions.

2. Rayleigh–Plesset bubble dynamics

2.1. Notation and parameters

Since Lord Rayleigh (1917, see Lamb 1932 for earlier references) treated the collapse of an empty cavity in a liquid, a lot of refinement has been done in the modelling of the dynamics of spherical domain walls in liquids. The main step towards bubble dynamics was the introduction of a variable external driving pressure and of the influence of surface tension by Plesset (1949).

An ODE for the bubble radius can be derived from the Navier–Stokes equations from an approximation valid to the order of \dot{R}/c_l , where \dot{R} is the speed of the bubble wall and c_l is the sound speed in the liquid. Following Prosperetti & Lezzi (1986), Löfstedt *et al.* (1993) and many others, we will henceforth denote the following ODE as Rayleigh–Plesset (RP) equation:

$$\begin{aligned} \rho_l \left(R \ddot{R} + \frac{3}{2} \dot{R}^2 \right) &= p_{gas}(R, t) - P(t) - P_0 \\ &+ \frac{R}{c_l} \frac{d}{dt} p_{gas}(R, t) - 4\eta_l \frac{\dot{R}}{R} - \frac{2\sigma}{R}. \end{aligned} \quad (2.1)$$

The left-hand side of this ODE for the bubble radius R consists of dynamical pressure terms already known to Rayleigh ($\rho_l = 1000 \text{ kg m}^{-3}$ is the density of water). $P_0 = 1 \text{ atm}$ is the constant ambient pressure, $P(t)$ the ultrasound driving, modelled as a spatially homogeneous, standing sound wave, i.e.,

$$P(t) = -P_a \cos \omega t = -P_0 \cdot p \cos \omega t \quad (2.2)$$

with the dimensionless forcing pressure amplitude $p \equiv P_a/P_0$ and a fixed frequency of $\omega = 2\pi \times 26.5 \text{ kHz}$ (period $T \approx 38 \mu\text{s}$), which is a common value in many experiments

like those of Barber *et al.* (1994) and Hiller *et al.* (1992). The wavelength of this sound in water is about 5 cm, while the bubble radii treated in this work never exceed 200 μm . Because of this separation of scales, it is common to assume spatial homogeneity, as stated above. We will refer to the sum of experimentally controllable pressures as the *external pressure* $p_{ext} = P_0 + P(t)$. By definition, the external pressure exerts maximally outward directed forces ($p_{ext} = P_0(1 - p) < 0$) on the bubble at $t = 0$.

The other terms on the right-hand side of equation (2.1) model the influence of the surface tension at the bubble-water interface ($\sigma = 0.073 \text{ kg s}^{-2}$), the water viscosity ($\eta_l = 1.00 \times 10^{-3} \text{ Pas}$), and of emitted sound waves from the bubble (cf. Keller & Miksis 1980, this term contains the speed of sound in water $c_l = 1481 \text{ m s}^{-1}$).

The gas pressure $p_{gas}(R, t)$ inside the bubble is assumed to obey a van der Waals type process equation

$$p_{gas}(R, t) = p_{gas}(R(t)) = \left(P_0 + \frac{2\sigma}{R_0} \right) \left(\frac{R_0^3 - h^3}{R^3(t) - h^3} \right)^\kappa, \quad (2.3)$$

R_0 being the ambient bubble radius and h the (collective) van der Waals hard core radius $h = R_0/8.86$ (for argon) (Lide 1991). The pressure exerted by surface tension was included explicitly in (2.1). The σ dependence of the prefactor of the polytropic expression ensures that R_0 is the radius of a static (unforced) bubble, neglecting effects of gas diffusion. Note that (2.3) presupposes homogeneity of the pressure inside the bubble. This is of course not satisfied in the final stages of bubble collapse, as a more detailed investigation of the gas dynamics inside the bubble reveals, cf. Wu & Roberts (1993), Moss *et al.* (1994), Vuong & Szeri (1996), Evans (1996), Brenner *et al.* (1996b), Moss *et al.* (1997), but the violent collapse phase lasts only $\sim 1 \text{ ns}$ out of the $T \approx 38 \mu\text{s}$ of the oscillation cycle. Therefore, this approximation does not severely affect our analysis of bubble wall dynamics. We furthermore set the effective polytropic exponent $\kappa \approx 1$ as for this frequency and bubble ambient radii below $\sim 20 \mu\text{m}$ the bubbles can be considered to be isothermally coupled to the surrounding liquid (Plesset & Prosperetti 1977), except during the small time interval around the bubble collapse, where the extremely rapid bubble dynamics requires adiabatic treatment of the gas. This will be taken into account in §§ 4.1 and 4.2. The solid line of figure 2(a) shows a time series $R(t)$ from (2.1) for relatively strong driving $P_a = 1.4 \text{ atm}$ and moderate ambient radius $R_0 = 4.0 \mu\text{m}$. The typical feature of the oscillations of $R(t)$ is a slow expansion for approximately half a cycle of driving, followed by a rapid and violent collapse and a series of afterbounces corresponding to an almost free oscillation of the bubble. The time scale of the afterbounces is thus set by the period of the bubble's (small amplitude) eigenoscillations, whose frequency $\omega_e \sim 1 \text{ MHz}$ can be easily obtained from a linearization of (2.1):

$$\ddot{R} + \omega_e^2(R - R_0) = \frac{P_a \cos \omega t}{\rho_l R_0} \quad \text{with} \quad (2.4)$$

$$\omega_e^2 = \frac{3P_0}{\rho_l R_0^2}, \quad (2.5)$$

where we have set $\kappa = 1$ and neglected surface tension and viscosity effects. Including

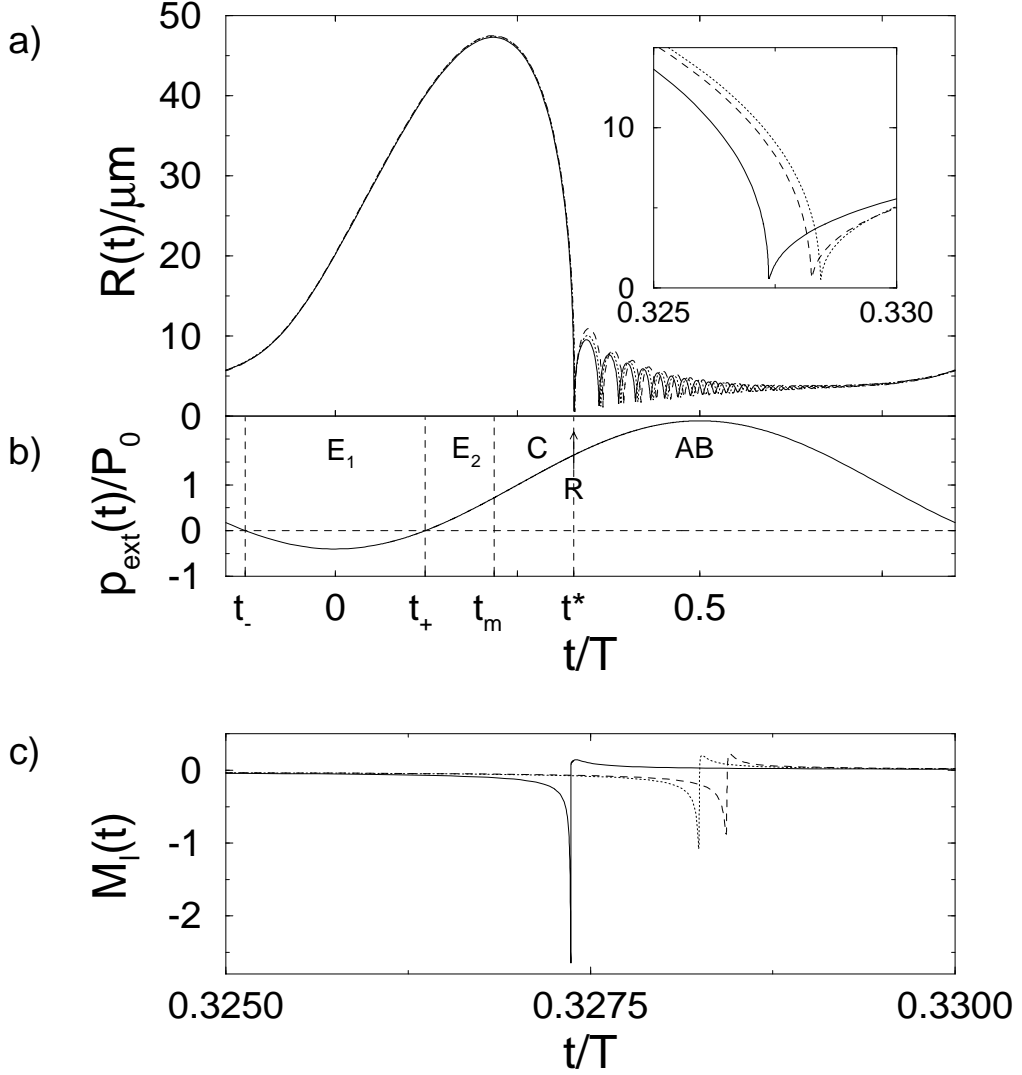


FIGURE 2. (a) Bubble dynamics for $P_a = 1.4 \text{ atm}$, $R_0 = 4.0 \mu\text{m}$ resulting from the RP equation (2.1) (solid), Flynn's equation (A 1) (dotted) and Gilmore's equation (A 2) (dashed). The inset shows a blowup of the vicinity of the collapse. (b) External pressure p_{ext} for the dynamics in (a). t_m is the time of maximum expansion, t^* the time of collapse; $p_{\text{ext}} = 0$ at $t = t_+, t_-$. The different intervals of the oscillation cycle treated in Section 4 are indicated. (c) Mach numbers M_l for the time interval displayed in the inset of (a). For the RP equation (solid) and Flynn's equation (dotted) $M_l = \dot{R}/c_l$ with constant c_l , for Gilmore's equation (dashed) $M_l = \dot{R}/C_l$ with pressure dependent C_l .

surface tension yields

$$\omega_s^2 = \frac{3P_0}{\rho_l R_0^2} + \frac{4\sigma}{\rho_l R_0^3} = \left(1 + \frac{2}{3}\alpha_s\right) \omega_e^2, \quad (2.6)$$

pressure term	definition
p_{acc}	$\rho_l R \ddot{R}$
p_{vel}	$\frac{3}{2} \rho_l \dot{R}^2$
p_{gas}	$(P_0 + \frac{2\sigma}{R_0}) \left(\frac{R_0^3 - h^3}{R^3 - h^3} \right)^\kappa$
p_{sur}	$\frac{2\sigma}{R}$
p_{vis}	$4\eta_l \frac{\dot{R}}{R}$
p_{snd}	$\frac{R}{c_l} \left(P_0 + \frac{2\sigma}{R_0} \right) \frac{d}{dt} \left(\frac{R_0^3 - h^3}{R^3 - h^3} \right)^\kappa$
p_{ext}	$P_0 - P_a \cos \omega t = P_0(1 - p \cos \omega t)$

TABLE 1. Definition of the pressure terms in the RP equation (2.1) used in this work.

where $\alpha_s = 2\sigma/(P_0 R_0)$ is the ratio of surface tension pressure to P_0 at $R = R_0$. $\alpha_s \approx 1$ for $R_0 \approx 1.5 \mu m$, while for larger R_0 it becomes very small.

The *resonance radius*, on the other hand, is defined as the ambient radius of a bubble with $\omega_e = \omega$, i.e.,

$$R_{res} = \left(\frac{3P_0}{\rho_l \omega^2} \right)^{1/2} \approx 105 \mu m. \quad (2.7)$$

For convenience, we list in table 1 the definition of the different pressure terms of (2.1) which will appear throughout this paper.

Besides the solution of the RP equation (2.1), figure 2(a) shows time series obtained from other commonly used bubble dynamical equations, namely Flynn's and Gilmore's equation, which are discussed in detail in Appendix A. It is obvious that, for bubbles in the SBSL regime, all equations yield very similar $R(t)$ dynamics. It is only upon magnification of the small time interval around the collapse (figure 2b) that the differences between these descriptions of bubble dynamics becomes apparent.

The deviations of the RP, Flynn, and Gilmore equations from each other may become pronounced when the bubble is driven at very high pressure amplitudes such as $P_a = 5 atm$ (cf. Lastman & Wentzell 1981). These pressures are common in cavitation fields, but they are far too high to allow for stable bubbles in SBSL experiments (with the possible exception of SBSL in high magnetic fields described by Young, Schmiedel & Kang 1996). Sonoluminescent bubbles require a driving pressure amplitude in a narrow window $1.1 atm \lesssim P_a \lesssim 1.5 atm$. It is this range of P_a that we will mainly focus on in this work. Only in § 4.4 results in the range of cavitation field pressures will briefly be displayed. Direct and indirect measurements of the size of SL bubbles e.g. in Barber & Puttermann (1992), Tian *et al.* (1996), or Holt & Gaitan (1996) indicate that typical R_0 lie around $5 \mu m$.

2.2. Calculating diffusive equilibria from RP dynamics

A computation of points of diffusive equilibrium in the P_a - R_0 plane from first principles requires solution of an advection diffusion PDE with appropriate boundary conditions, coupled to the RP equation. This is numerically far too expensive to allow for

a scan of the whole P_a - R_0 parameter space. In Brenner *et al.* (1996a) and Hilgenfeldt *et al.* (1996), we therefore employed the method introduced by Fyrillas & Szeri (1994) and Löfstedt *et al.* (1995), which is based on the separation of the driving time scale T and the diffusive time scale $\tau_{diff} \gg T$. Within this approximation, the task is massively reduced to the solution of the RP equation and the computation of weighted averages of the form

$$\langle f \rangle_i = \int_0^T f(t) R^i(t) dt \Bigg/ \int_0^T R^i(t) dt. \quad (2.8)$$

The mass flux into or out of the bubble is then proportional to $p_\infty - \langle p_{gas} \rangle_4$ (see Fyrillas & Szeri 1994). An equilibrium point is characterized by the simple condition

$$p_\infty = \langle p_{gas} \rangle_4 \quad (2.9)$$

and it is stable if

$$\beta = \frac{d \langle p_{gas} \rangle_4}{d R_0} \quad (2.10)$$

is positive.

Figure 3a displays $\langle p_{gas} \rangle_4$ for different P_a . The graphs show characteristic wiggles for larger R_0 (which can be explained from resonance effects, see § 4.3) and, for large enough P_a , a global *minimum* at some critical $R_0 = R_0^c$. If $R_0 > R_0^c$, even with no wiggles present, the bubbles are diffusively stable according to the sign of the slope β . For small $R_0 < R_0^c$, all equilibria are unstable, i.e., the bubble either dissolves or grows by rectified diffusion, see Blake (1949), Eller & Flynn (1964) (the latter case can lead to unstable SBSL, cf. Hilgenfeldt *et al.* 1996). The possibility of multiple stable equilibria because of the resonance structure was recognized earlier by Church (1988) and Kamath, Prosperetti & Egolfopoulos (1993). Here we analyse the formal and physical origin of the positive *overall* slope of $\langle p_{gas} \rangle_4(R_0)$ for large R_0 , which is an essential property of stable SBSL bubbles.

In the average $\langle p_{gas} \rangle_4$ the pressure is weighted with $R^4(t)$ and will therefore be dominated by the value of p_{gas} at R_{max} . For large radii, we can neglect the excluded volume h^3 in the van der Waals formula and replace (2.3) by an ideal gas law under isothermal conditions,

$$\frac{\langle p_{gas} \rangle_4}{P_0} \approx (1 + \alpha_s) \frac{\int_0^T R_0^3 R(t) dt}{\int_0^T R^4(t) dt} \approx \xi (1 + \alpha_s) \left(\frac{R_0}{R_{max}} \right)^3. \quad (2.11)$$

ξ is a prefactor that is due to the different shape of the integrands $R(t)$ and $R^4(t)$. A crude estimate of ξ can be obtained by approximating $R(t)$ by a parabola $\tilde{R}(t) \sim R_{max}(1 - 16t^2/T^2)$ and integrating \tilde{R} and \tilde{R}^4 over one half cycle from $-T/4$ to $T/4$. This gives $\xi = 105/64 \approx 1.64$, which is quite accurate in reproducing numerical results. With this saddle point approximation introduced by Löfstedt *et al.* (1993), the key parameter for diffusive equilibria is the expansion ratio R_{max}/R_0 . Figure 3 demonstrates the close relation between $\langle p_{gas} \rangle_4$ and R_{max}/R_0 as functions of R_0 . The expansion ratio displays a maximum at R_0^c , corresponding to the minimum of $\langle p_{gas} \rangle_4$. In order to determine

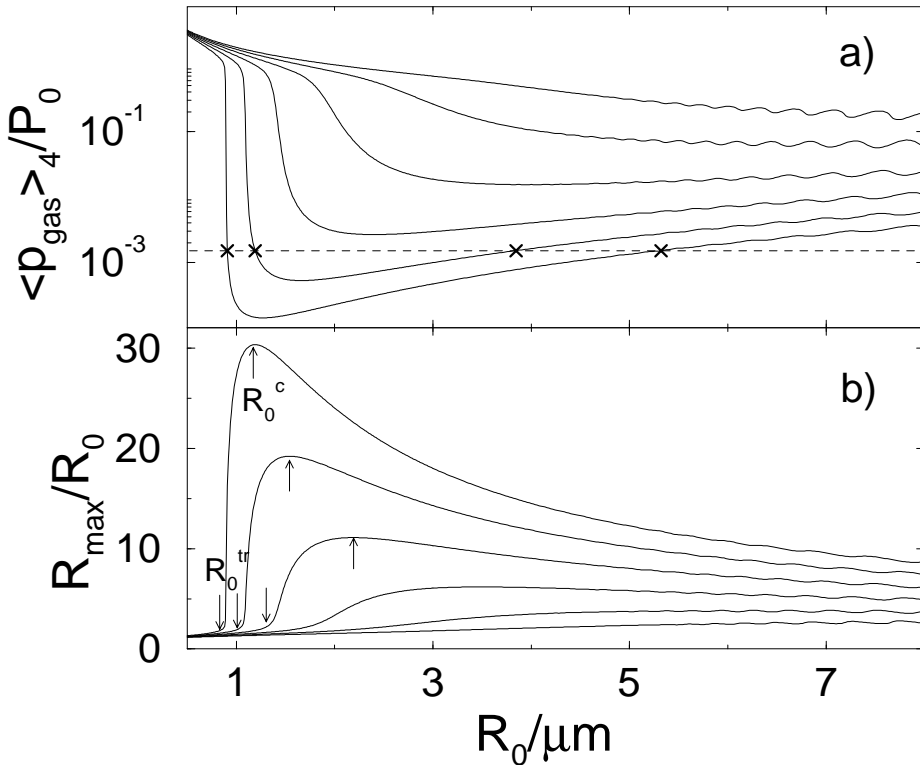


FIGURE 3. (a) Average pressure $\langle p_{\text{gas}} \rangle_4$. The curves are parametrized with the dimensionless driving pressures $p = 1.0, 1.1, 1.2, 1.3, 1.4$, and 1.5 from top to bottom. Note the logarithmic scale of the ordinate. The horizontal dashed line is an example for a given gas concentration p_∞ / P_0 in the liquid. Crosses mark the corresponding R_0 where diffusive equilibria are found. (b) Expansion ratio R_{max} / R_0 for the same p as in (a): $p = 1.0$ to 1.5 in steps of 0.1 from bottom to top. The maxima occur at almost exactly the same $R_0 = R_0^c$ as the minima of $\langle p_{\text{gas}} \rangle_4$. Up arrows mark the R_0^c , down arrows indicate the transition radii R_0^{tr} for $p=1.3, 1.4, 1.5$.

diffusive equilibrium points, one has to look for the intersections of the $\langle p_{\text{gas}} \rangle_4 / P_0$ curves in figure 3 with a horizontal line given by p_∞ / P_0 (cf. equation (2.9)). Note that degassing to tiny partial pressures is necessary to achieve equilibria in the R_0 range of pure argon SL bubbles; this fact was first realized by Löfstedt *et al.* (1995).

For high enough P_a , there are two equilibrium values for R_0 , the larger one being a stable equilibrium, the smaller one being unstable. If P_a is decreased, $\langle p_{\text{gas}} \rangle_4 / P_0$ increases and the equilibria come closer together. This can also be seen in figure 1: for decreasing P_a , the R_0 values given by the $p_\infty / P_0 = 0.002$ equilibrium curve approach each other. Eventually, at a certain P_a the stable und the unstable equilibrium coalesce and for smaller P_a no equilibrium is possible. This is reflected in figure 3 by the fact that the whole $\langle p_{\text{gas}} \rangle_4 / P_0$ curve lies above p_∞ / P_0 .

For relatively high gas concentrations such as $p_\infty / P_0 = 0.2$, stable equilibria can only

exist for very large R_0 , where the bubbles are shape unstable. But if the concentration is lowered, e.g. to $p_\infty/P_0 = 0.002$, the stable branch (positive slope in figure 1) enters the region of sonoluminescent bubbles, whereupon stable SL can set in. The occurrence of stable and unstable branches depends on the existence of a minimum in $\langle p_{\text{gas}} \rangle_4$, which in turn necessitates a maximum in R_{max}/R_0 (figure 3a and b). Therefore, to analyse the lines of diffusive equilibria in figure 1, it is sufficient to explain the maximum of the expansion ratio figure 3(b) and its dependence on R_0 and p ; this question will be addressed in § 4.4.

3. Quasistatic Blake threshold

The transition from sharply increasing R_{max}/R_0 for small R_0 to decreasing expansion ratios for large R_0 (figure 3b) marks an important boundary between two very different types of bubble dynamics. Consider figure 4 where two examples of bubble dynamics for the same $P_a = 1.5 \text{ atm}$ and only minutely different ambient radii are displayed. The smaller bubble exhibits a weak (although obviously not sinusoidal) oscillation with a maximum expansion ratio $R_{\text{max}}/R_0 \approx 2$; no collapse is visible. The time series of the larger bubble is almost indistinguishable from the other until $t \approx 0$. But then, a rapid expansion to $R_{\text{max}}/R_0 \approx 10$ occurs, followed by a strong collapse, the typical dynamics of a sonoluminescing bubble, cf. figure 2(a).

Figure 5 shows the compression ratio R_{min}/R_0 of the minimum radius achieved during bubble oscillation to the ambient radius as a function of P_a and R_0 . A sharp transition, like in the expansion ratio, is obvious in this graph and it occurs at the same R_0 . For small P_a and small R_0 , R_{min}/R_0 is near one; we denote such bubbles as *weakly oscillating*. For large P_a and R_0 , a horizontal plane at $R_{\text{min}}/R_0 \approx h/R_0$ indicates collapse to a radius very near the hard core radius. We say that these latter bubbles exhibit *strong collapses*.

The key to understanding this transition from weakly oscillating to strongly collapsing bubbles lies in the existence of a threshold for spontaneous bubble expansion known as the Blake threshold (Blake 1949, Atchley 1989). It is normally considered for bubbles under static conditions: let us first set P_a (and thus also p_{ext}) constant in time, and correspondingly take $R(t)$ to be time-independent. Then the RP equation reduces to

$$0 = (P_0 + \frac{2\sigma}{R_0}) \left(\frac{R_0}{R} \right)^3 - p_{\text{ext}} - \frac{2\sigma}{R}, \quad (3.1)$$

where for p_{gas} again the isothermal ideal gas law was used, which is certainly an excellent approximation for the static situation. For $p_{\text{ext}} > 0$, equation (3.1) has exactly one solution for positive R , and it corresponds to a stable equilibrium. If $p_{\text{ext}} < 0$ but small in absolute magnitude, two equilibria exist, the one at larger R being unstable, i.e., a bubble with larger radius would grow indefinitely. Finally, at a critical $p_{\text{ext}}^B < 0$ (Blake threshold pressure, cf. Prosperetti 1984) the two equilibrium points merge and disappear in an inverse tangent bifurcation. In this situation, p_{gas} is always larger than $p_{\text{ext}} + p_{\text{sur}}$ and (3.1) cannot be fulfilled for any radius. Thus, the assumption of a time-independent

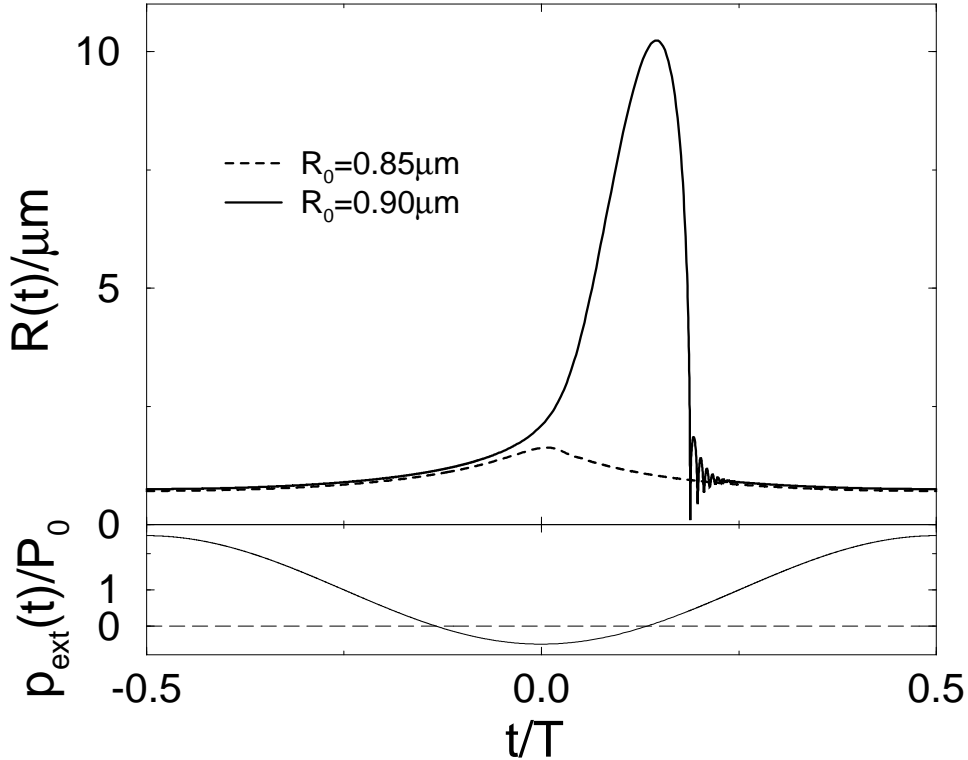


FIGURE 4. Bubble dynamics for $P_a = 1.5\text{ atm}$, $R_0 = 0.85\mu\text{m}$ (dashed) and $R_0 = 0.90\mu\text{m}$ (solid). The larger bubble undergoes dynamical expansion and a strong collapse, the smaller oscillates weakly with the driving field (lower part).

$R(t)$ has to be dropped. A dynamical expansion ensues with significant contributions from the dynamical pressure terms on the left-hand side of (2.1).

Returning to the oscillatory driving $p_{\text{ext}} = P_0(1 - p \cos \omega t)$, we notice that the driving period $T = 2\pi/\omega \approx 40\mu\text{s}$ is long compared to the time scale of the bubble's eigenoscillations $2\pi/\omega_e \sim 1\mu\text{s}$. Thus, we can consider the external pressure oscillations as quasistatic and follow Blake's argument as above. As $p_{\text{ext}} < 0$ is necessary to cross the Blake threshold, we must require $p > 1$ here. Obviously, the most sensitive point in the cycle is $t = 0$, where p_{ext} is negative and of magnitude $(p - 1)P_0$.

The quasistatic approximation (3.1) describes the *complete* time series of a weakly oscillating bubble with good accuracy. Rewriting (3.1), we obtain the cubic equation

$$(p \cos \omega t - 1)R^3 - \frac{2\sigma}{P_0}R^2 + \left(1 + \frac{2\sigma}{R_0 P_0}\right)R_0^3 = 0. \quad (3.2)$$

Given a time t for which $p_{\text{ext}} < 0$, there is a critical $R_0 = R_0^{tr}$ above which the two positive real solutions of (3.2) become complex. When this happens, the weak oscillation dynamics is no longer a valid description and the transition to strong collapses occurs.

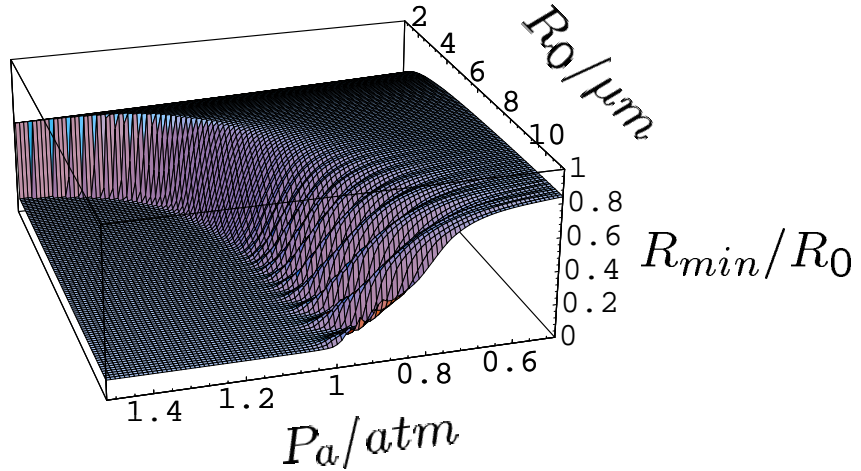


FIGURE 5. Compression ratio R_{min}/R_0 as a function of P_a and R_0 . The two regimes of bubble dynamics are clearly visible: weakly oscillating bubbles for small R_0 and small P_a , strong collapses to the hard core radius for large R_0 and large P_a .

For given p , the smallest transition radius R_0^{tr} is required for $t = 0$. For R_0^{tr} , therefore, the discriminant of (3.2) at $t = 0$ must vanish, i.e.,

$$R_0^3 + \frac{2\sigma}{P_0} R_0^2 - \frac{32}{27} \frac{\sigma^3}{P_0^3 (p-1)^2} = 0. \quad (3.3)$$

After a lengthy but straightforward calculation, the transition ambient radius R_0^{tr} at given $p = P_a/P_0$ is

$$R_0^{tr} = \frac{2}{3} \frac{\sigma}{P_0} \left\{ \left(\frac{2}{(p-1)^2} - 1 + \frac{2}{(p-1)} \sqrt{\frac{1}{(p-1)^2} - 1} \right)^{1/3} + \left(\frac{2}{(p-1)^2} - 1 + \frac{2}{(p-1)} \sqrt{\frac{1}{(p-1)^2} - 1} \right)^{-1/3} - 1 \right\}. \quad (3.4)$$

Note that R_0^{tr} is a real number for all p . In figure 6 the calculated R_0^{tr} from (3.4) is compared to the numerical values (identified by the condition $R_{min}/R_0 = 0.5$). The agreement is very good, the errors at higher P_a being only about $0.01 \mu\text{m}$.

When R_0 exceeds R_0^{tr} , there is a period of time around $t = 0$ where the right-hand side of (3.1) cannot be zero, but must be positive. Then, the dynamical terms neglected so far must become noticeable and a dynamical expansion follows which can only be stopped when p_{ext} has again become large enough to allow for a stable radius equilibrium. When the bubble growth is stopped, the expanded bubble does not experience significant outward directed forces and, consequently, undergoes a violent collapse. If R_0 is only

slightly larger than R_0^{tr} , the time scale separation still holds for a large portion of the cycle, cf. figure 4.

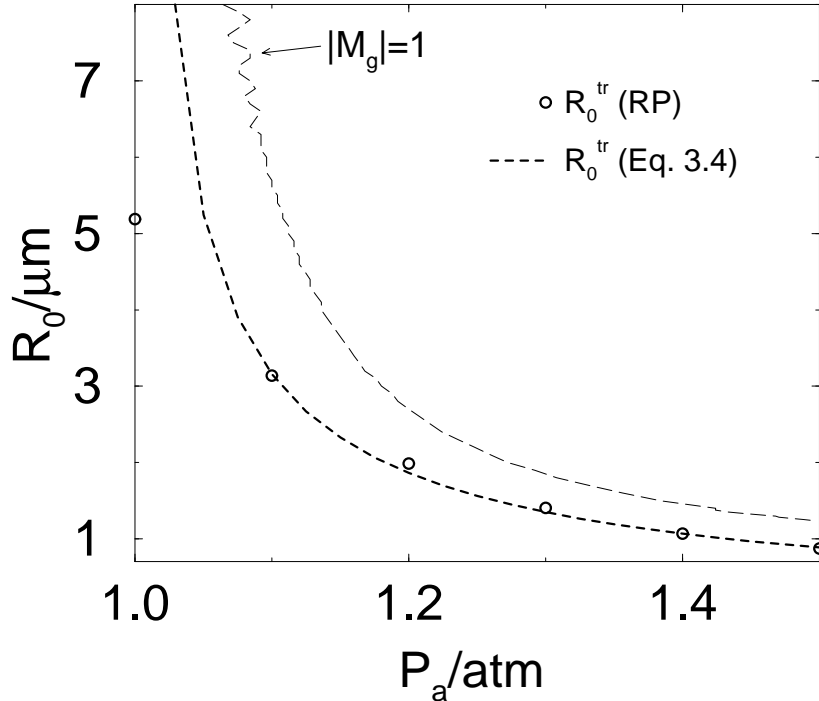


FIGURE 6. Transition ambient radii R_0^{tr} from numerical solution of the RP ODE (circles) and from (3.4) (dashed). This figure shows the same parameter range as figure 1, from which the $|M_g| = 1$ curve was taken (thin dashed line). The transition to collapsing bubbles occurs for slightly smaller pressures and ambient radii than the onset of light emission at $|M_g| = 1$.

It is immediately obvious from (3.3) and (3.4) that surface tension plays a key role in this transition mechanism from weak oscillations to strong collapses. If $p > 1$, weak oscillations at small R_0 are dominated by the influence of σ , whereas strongly collapsing (larger) bubbles are controlled by the properties of dynamical expansion and collapse (cf. §§ 4.1, 4.4). Note that in a fluid with very small σ , already bubbles of very small size will show collapses (see also Löfstedt *et al.* 1995 and Akhatov *et al.* 1997). It should also be emphasized here that the crucial driving parameter for the transition is $(p - 1)$, i.e., the *difference* of driving pressure amplitude P_a and ambient pressure P_0 , rather than P_a itself.

In the limit of large forcing $p \gg 1$, (3.3) yields the much simpler formula

$$R_0^{tr} = \frac{4}{9} \sqrt{3} \frac{\sigma}{P_0} \frac{1}{p - 1}. \quad (3.5)$$

It can be seen from figure 3 that in this limit the difference between R_0^{tr} (onset of transition) and R_0^c (extremum of expansion and compression ratio) becomes negligibly small. Thus, (3.5) is also a good approximation to the critical R_0^c we were trying to identify. This is confirmed by figure 7, from which also the (small) errors of the saddle point approximation (determining R_0^c from R_{max}/R_0 instead of $\langle p_{gas} \rangle_4$) can be read off.

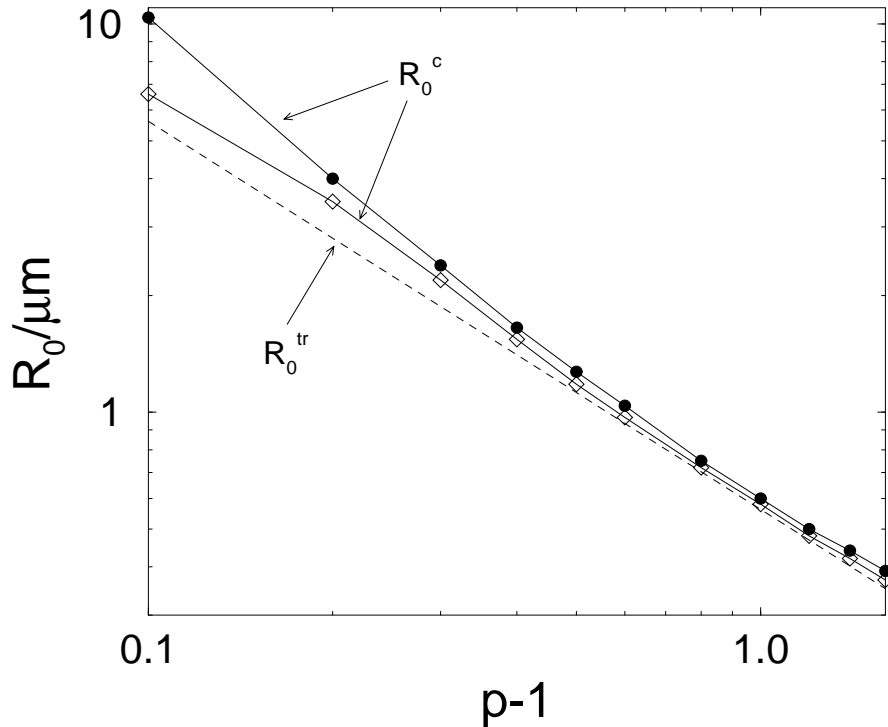


FIGURE 7. Critical ambient radii R_0^c from numerical computation of the extrema of $\langle p_{gas} \rangle_4$ (filled circles) and R_{max}/R_0 (open diamonds) and from the asymptotic law for R_0^{tr} equation (3.5) (dashed line). The scaling behaviour $R_0^c \propto 1/(p-1)$ from (3.5) is quite accurate for higher pressures $p \gtrsim 1.3$.

What is the maximum radius of a bubble weakly oscillating at $R_0^{tr}(p)$? Inserting (3.5) into (3.2) with $t = 0$ and expanding to the same order in $1/(p-1)$ gives

$$R_{max} = \frac{4}{3} \frac{\sigma}{P_0} \frac{1}{p-1} \quad (3.6)$$

in the large p limit. This yields a minimum expansion ratio of $R_{max}/R_0^{tr} = \sqrt{3}$ for the onset of bubble collapse, which is an analytical justification of Flynn's (1975b) definition of a *transient cavity*. In that work, a strongly collapsing bubble was characterized by an expansion ratio $\gtrsim 2$.

As the collapse sets in rather abruptly when R_0 is enlarged, we expect that R_0^{tr} also

marks the transition to bubbles which fulfill the Mach criterion (1.1). Figure 6 shows the $|M_g| = 1$ line of figure 1 together with the $R_0^{tr}(p)$ line according to (3.4). Both curves display the same trend, approaching each other at large p . The Blake transition occurs for smaller P_a and R_0 than those necessary for $|M_g| \gtrsim 1$, i.e., for possible light emission. The physical consequence of this is that, upon increasing the driving force, the bubble first emits cavitation noise due to collapses and only afterwards starts to emit light. Indeed, such a sequence of events has been reported by W. Eisenmenger & B. Gompf (private communication, 1996).

The transition line $R_0^{tr}(p)$ is shifted towards smaller R_0 for smaller σ . This means that collapses of the same violence can be achieved (for a given R_0 range) with smaller driving pressures in a liquid with less surface tension. Note however that such bubbles will also be stronger affected by surface instabilities, whereas in a liquid with high σ , bubbles are more surface stable. It is therefore possible to obtain violent collapses at larger R_0 in liquids with larger surface tension using larger driving pressures.

4. A guided tour of RP dynamics

Let us now explain in detail the dynamics of strongly collapsing bubbles (as shown e.g. in figure 2a). To this end, we divide the oscillation cycle of the bubble into several time intervals indicated in figure 2(b), where t_m is the time of maximum bubble radius, t^* the time of minimum bubble radius (after collapse), and $t_+ = -t_- = \arccos(1/p)/\omega$ the time when p_{ext} changes its sign from positive (contracting) to negative (expanding) values. With this interval division scheme we extend an approach presented in the pioneering paper by Löfstedt *et al.* (1993). In particular, we will treat the *bubble collapse phase* denoted by C in figure 2(b) in the interval $t_m \leq t \leq t^*$, the *reexpansion interval* (R) very close to the time of maximum compression ($t \approx t^*$), the *afterbounces* (AB) for $t^* \leq t \leq t_-$ and the *bubble expansion* in two stages for $t_- \leq t \leq t_+$ (E₁) and $t_+ \leq t \leq t_m$ (E₂).

Within each of these intervals, certain pressure terms in (2.1) are dominant, whereas others are negligible. Thus, simplified equations with analytical solutions can be derived, which enable us to characterize the complex bubble behaviour analytically and quantitatively. Our approximate formulas hold in the regime of strongly collapsing bubbles, i.e., for $R_0 > R_0^{tr}(P_a)$; in the weakly oscillating regime, the bubble dynamics becomes of course trivial.

4.1. Rayleigh collapse (region C)

We first take a closer look at the main collapse (after R_{max} has been reached, interval C in figure 2b). Figure 8 shows the behaviour of the most important terms in the RP equation (defined in table 1) just prior to the main collapse. The abscissa displays the logarithm of the time interval before the collapse time t^* which is identified by the condition $\dot{R}(t^*) = 0$, i.e., the bubble reaches its minimum radius at t^* . The ordinate gives the logarithms of the absolute values of the various pressure contributions. As the whole time interval treated in this subsection only comprises $\approx 0.1 \mu s$, and we want to discuss processes as

fast as 1 ns , we choose the polytropic exponent in (2.3) to be $\kappa = 5/3$, the adiabatic value for argon. Note that the portions of the graphs for $|t^* - t| \lesssim 10^{-7}T$ in figure 8, as well as in figures 9 – 11 below, represent time scales on or below the picosecond scale. As hydrodynamics breaks down here, this part of the computation will only be able to give a reasonable effective dynamics. We will take care not to draw physical conclusions from data in this range.

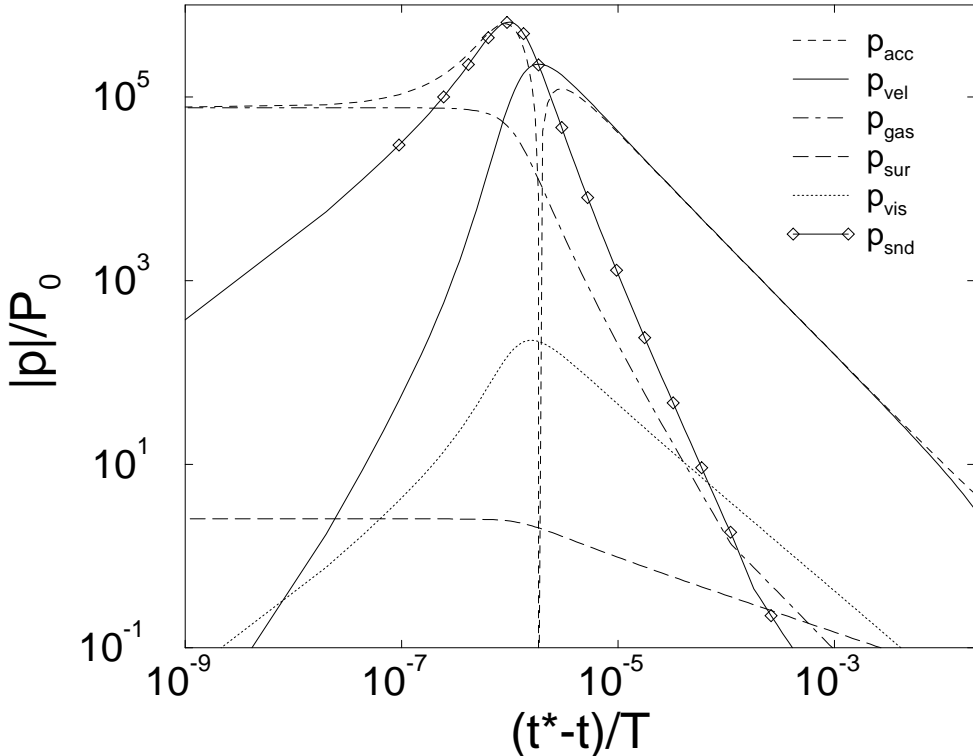


FIGURE 8. Relevant pressure contributions according to the complete RP equation on a log-log scale before the instant of collapse t^* . The bubble is driven at $P_a = 1.4\text{ atm}$ and its ambient radius is $R_0 = 4\text{ }\mu\text{m}$.

In a large part of the collapse phase (figure 8) the dynamical terms p_{acc} and p_{vel} give the dominant contribution; they compensate each other, so that the dynamics is well described by the classical Rayleigh collapse

$$R\ddot{R} + \frac{3}{2}\dot{R}^2 = 0. \quad (4.1)$$

This formula complements the quasistatic approximation (3.1) above. Equation 4.1 implies a scaling law for $R(t)$:

$$R(t) = R_R \left(\frac{t^* - t}{T} \right)^{2/5}. \quad (4.2)$$

Here, the oscillation period T is used for non-dimensionalization of the time coordinate. The characteristic radius R_R can be estimated from an energy argument: at $R = R_{max}$, the potential energy of the bubble is approximately $E_{pot} \sim 4\pi P_0 R_{max}^3/3$, see e.g. Smereka, Birnir & Banerjee (1987). Converting this into kinetic energy of the fluid at $R = R_0$, we get as an estimate for the bubble wall speed at $R = R_0$

$$\dot{R}|_{R=R_0} = -\left(\frac{2P_0}{3\rho_l}\right)^{1/2} \left(\frac{R_{max}}{R_0}\right)^{3/2}. \quad (4.3)$$

Using the time derivative of (4.2), we find

$$R_R = R_0 \left(\frac{5T|\dot{R}|_{R=R_0}}{2R_0}\right)^{2/5} = \left(\frac{25P_0T^2}{6\rho_l}\right)^{1/5} R_{max}^{3/5} \approx 14.3 \mu m \cdot \left(\frac{R_{max}}{\mu m}\right)^{3/5}. \quad (4.4)$$

With this R_R , (4.2) is compared to the numerical result of the RP ODE in figure 9. Both slope and prefactor are reproduced excellently, despite the rather crude approximations leading to (4.4). The only characteristic value for the Rayleigh collapse is R_{max} , which depends on P_a and (although weakly) on R_0 . Analytical expressions for these dependences will be given in Section 4.4.

We now examine the range of validity of (4.1); one could worry whether it is justified to neglect p_{gas} and p_{snd} during collapse. For the solution (4.2), we have $p_{vel} = -p_{acc} \propto (t^* - t)^{-6/5}$, whereas (as long as $R(t)^3 \gg h^3$) $p_{gas} \propto (t^* - t)^{-2}$ and $p_{snd} \propto (t^* - t)^{-13/5}$ for $\kappa = 5/3$, i.e., the latter two pressure contributions grow stronger than the dynamical terms as $t \rightarrow t^*$. This can also be observed in figure 8, but the absolute value of p_{gas} and p_{snd} is negligible compared to p_{vel}, p_{acc} except for times very close to t^* . We can compute the range of validity of (4.1) by equating $p_{gas} = p_{vel}$ and $p_{snd} = p_{vel}$, respectively, using (4.2), (4.4). It turns out that the sound pressure contribution is the first to violate (4.1). This happens at t_{snd} with

$$\begin{aligned} (t^* - t_{snd})/T &= \left(\frac{192\rho_l c_l^2}{25P_0}\right)^{1/7} \frac{R_0}{c_l T} (1 + \alpha_s)^{5/7} \left(\frac{R_0}{R_{max}}\right)^{18/7} \\ &\approx 1.0 \times 10^{-4} (1 + \alpha_s)^{5/7} \left(\frac{R_0}{R_{max}}\right)^{18/7} \left(\frac{R_0}{\mu m}\right), \end{aligned} \quad (4.5)$$

which agrees with the numerical result e.g. in figure 8 (where $R_0 = 4 \mu m$ and $R_{max} \approx 47 \mu m$). For the approximation (4.5), $R^3(t_{snd}) \gg h^3$ was assumed; α_s is the surface tension parameter introduced in (2.6). The collapse behaviour changes due to p_{snd} shortly before another assumption for (4.1) breaks down: obviously, $R(t)$ cannot be smaller than the van der Waals hard core h . Equating $R(t) = h$ using (4.2) with $h = R_0/8.86$, we obtain the ‘‘hard core time’’

$$(t^* - t_{vdw})/T = \left(\frac{6\rho_l}{25P_0}\right)^{1/2} \frac{1}{T} \frac{h^{5/2}}{R_{max}^{3/2}} \approx 5.5 \times 10^{-6} \left(\frac{R_0}{R_{max}}\right)^{3/2} \left(\frac{R_0}{\mu m}\right). \quad (4.6)$$

At $t \approx t_{vdw}$, the van der Waals hard core cuts off the scaling behaviour abruptly. However, for typical values of $R_0 \approx 4 \mu m$, the bubble collapses like an empty cavity for a time interval from $(t^* - t) \sim 1 \mu s$ down to $(t^* - t) \sim 100 ps$ ($t^* - t \sim 0.03T \dots 3 \times 10^{-6}T$).

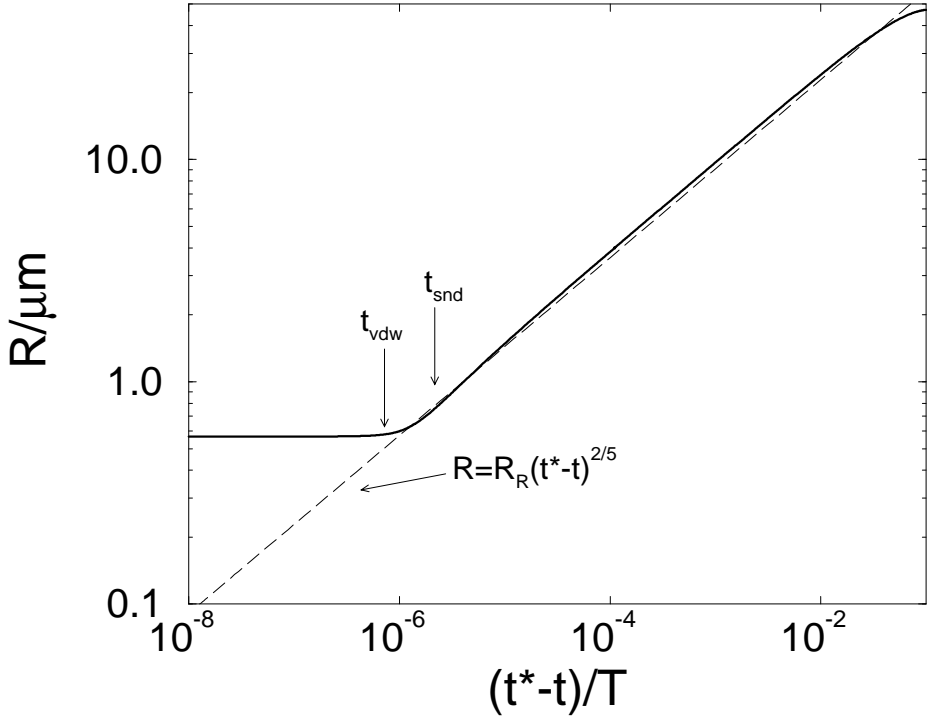


FIGURE 9. Collapse dynamics of $R(t)$ for the same parameters as in figure 8. This bubble reaches a maximum radius $R_{max} \approx 47 \mu\text{m}$ before collapsing. The theoretically expected Rayleigh scaling law $R(t) = R_R(t^* - t)^{2/5}$ (dashed) is followed accurately. Also indicated are the limiting times t_{vdw}, t_{snd} for the validity of the scaling law.

4.2. Turnaround and delayed reexpansion (region R)

As the gas is compressed to the hard core radius, the collapse is halted abruptly. Löfstedt *et al.* (1993) have shown that – in the Hamiltonian limit neglecting $p_{sur}, p_{vis}, p_{snd}$ and the temporal variation of p_{ext} – the turnaround time interval of the bubble is approximately

$$\tau_{turn} \equiv \left(\frac{R(t^*)}{\ddot{R}(t^*)} \right)^{1/2} \approx \left[3^\kappa \frac{\rho_l h^2}{P_0(1 + \alpha_s)} \left(\frac{h}{R_0} \right)^{3\kappa} \left(\frac{R_{min} - h}{h} \right)^\kappa \right]^{1/2}. \quad (4.7)$$

This equation also follows from approximating the RP equation (2.1) by keeping only the dominant terms in the immediate vicinity of the collapse, i.e., p_{acc} and p_{gas} (cf. figures 8 and 10):

$$\rho_l R \ddot{R} = P_0 (1 + \alpha_s) \left(\frac{R_0^3 - h^3}{R^3(t) - h^3} \right)^\kappa. \quad (4.8)$$

(4.8) is a good description of bubble dynamics for a time interval around the collapse of length $\sim \tau_{turn}$.

Figure 10 shows the pressure contributions *after* t^* . From $(t - t^*)/T \sim 10^{-6}$ to

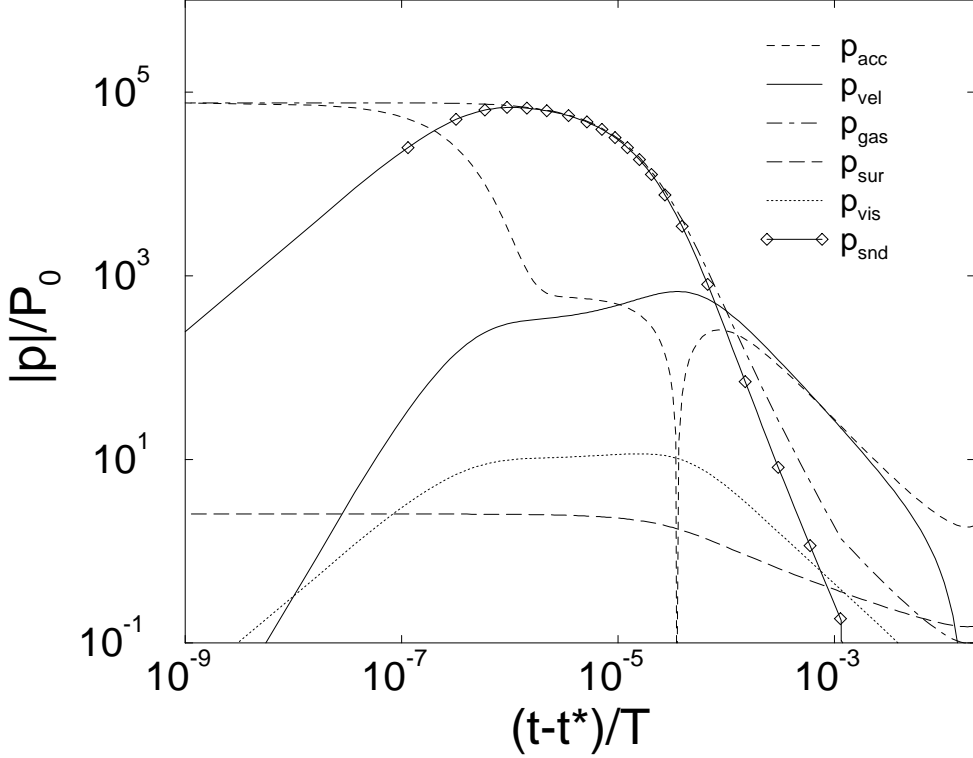


FIGURE 10. Important pressure contributions according to the RP equation on a log-log scale after the instant of collapse. The same parameters as in figure 8 apply.

$(t - t^*)/T \sim 10^{-4}$ (i.e., from $(t - t^*) \sim 30\text{ ps}$ to $\sim 3\text{ ns}$) the dominant terms in (2.1) are p_{gas} and p_{snd} , which compensate each other. This means that the energy stored in the compressed gas is released almost exclusively through emission of sound waves (cf. Church 1989) – it is not converted back to kinetic energy of the liquid surrounding the bubble. The corresponding dynamics shows a relatively low expansion velocity and small acceleration, keeping a very small bubble radius for a few ns (figure 11). This time interval of *delayed reexpansion* (denoted by R in figure 2b) is described by

$$0 = p_{\text{gas}}(R(t)) + \frac{R(t)}{c_l} \frac{d}{dt} p_{\text{gas}}(R(t)) \quad (4.9)$$

with p_{gas} given by (2.3). This ODE has an analytical solution :

$$\frac{c_l}{3\kappa} (t - t^*) = \left[R + \frac{h}{6} \ln \frac{(R - h)^2}{R^2 + h^2 + Rh} - \frac{h}{\sqrt{3}} \arctan \frac{2R + h}{\sqrt{3}h} \right]_{R_{\min}}^{R(t)}. \quad (4.10)$$

For $(R(t) - R_{\min}) \ll R_{\min}$, i.e., just after the collapse, this implicit equation can be simplified to yield

$$R(t) \approx R_{\min} + \frac{c_l}{3\kappa} \frac{R_{\min}^3 - h^3}{R_{\min}^3} (t - t^*). \quad (4.11)$$

This linear expansion law holds for a longer time interval if R_{min} is larger, i.e., for smaller P_a . Its validity is demonstrated in figure 11. Note that although the turnaround time τ_{turn} becomes smaller for decreasing $R_{min} - h$, the velocity of the bubble immediately after collapse is actually *smaller* because of the larger energy losses through acoustic radiation. The strongly asymmetric shape of $R(t)$ around t^* has also been observed in experimental measurements of bubble dynamics, e.g. by Barber & Puttermann (1992), Tian *et al.* (1996), Weninger, Barber & Puttermann (1997), and Matula *et al.* (1997).

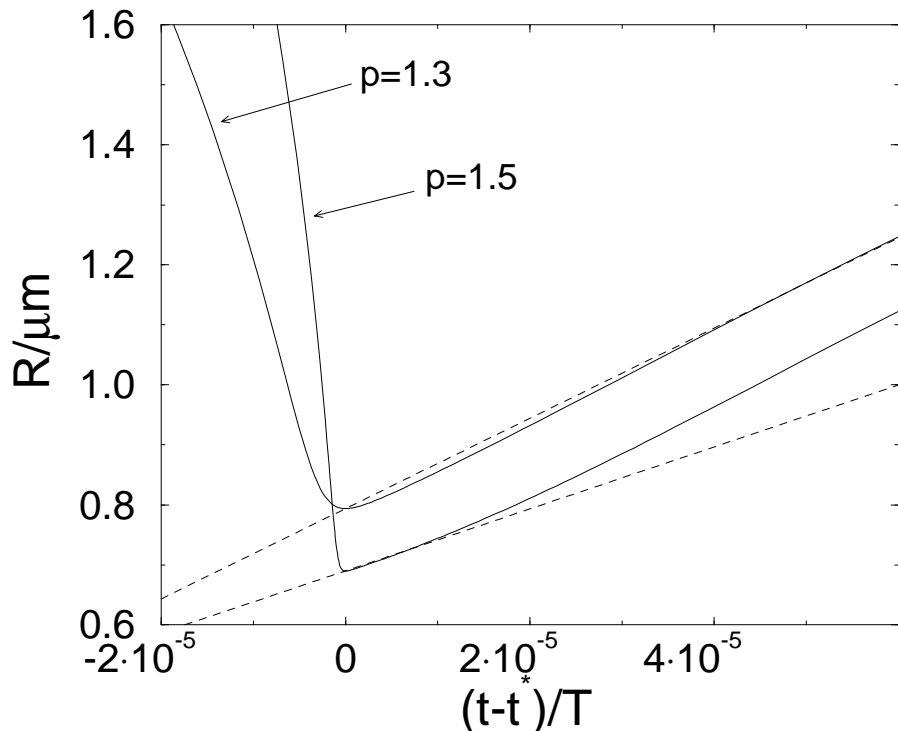


FIGURE 11. Bubble dynamics for $R_0 = 5 \mu\text{m}$ and two different driving pressure amplitudes $p = 1.3$ and $p = 1.5$ in the vicinity of collapse. The dashed lines give the linear reexpansion approximation from equation (4.11).

After the delayed reexpansion phase, the bubble wall gains speed and enters another short time interval around $(t - t^*) \approx 10^{-3}T$ well described by Rayleigh's equation (4.1) with $R(t) \propto (t - t^*)^{2/5}$ as the bubble expands. At $(t - t^*) \approx 10^{-2}T$ it enters the phase of subsequent afterbounces.

4.3. Afterbounces: a parametric resonance (region AB)

The discussion of the afterbounce interval (AB in figure 2b) is intimately connected to the explanation of the wiggly structure of various dynamically computed terms, like the expansion ratio (figure 3b) or the diffusive equilibrium lines in Fig 1. Obviously,

as the RP equation (2.1) describes a driven oscillator, the maxima in the expansion ratio represent parameter values of resonant driving. Figure 12 clarifies the character of these resonances. It shows two time series of the bubble radius $R(t)$ at values of R_0 corresponding to a relative maximum and a relative minimum of R_{max}/R_0 , respectively. A large or small expansion ratio results from the phase of the afterbounces at the time when p_{ext} becomes negative, i.e., when the external forces start the rapid expansion: for the bubble with the large expansion ratio, the last afterbounce “fits” into the expansion, which is enhanced. For the other bubble, growth is inhibited as the last afterbounce collapses with the expanding external force.

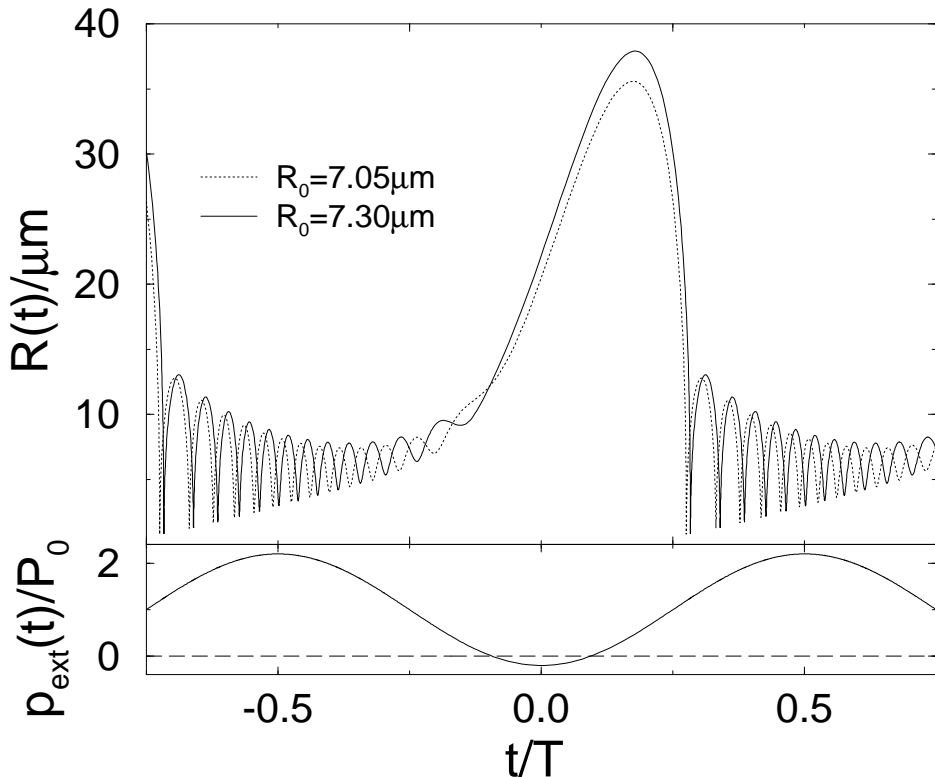


FIGURE 12. Two time series $R(t)$ for $P_a = 1.2 \text{ atm}$ and $R_0 = 7.05 \mu\text{m}$ (dashed), $R_0 = 7.30 \mu\text{m}$ (solid). The first ambient radius corresponds to a resonance minimum in R_{max}/R_0 , the second to a maximum. Note that the afterbounces at the beginning of the main expansion are just one half-cycle out of phase.

The afterbounce oscillations show relatively small amplitude, and it is therefore possible to linearize the RP equation in this region of the driving cycle. Moreover, sound radiation and viscosity contributions are negligible. For simplicity, we also neglect p_{sur} for the moment. In order to separate the time scale $1/\omega$ of the driving from the much shorter time scale of the afterbounces, which is $\sim 1/\omega_e$, we use the ansatz (cf. e.g.

Hinch 1991)

$$R(t) = \tilde{R}_0(\tau)(1 + y(t)) \quad (4.12)$$

with small $y(t)$ and a slowly varying function $\tilde{R}_0(\tau)$ which is to be determined; $\tau = \epsilon t$, $\epsilon = \omega_e/\omega_e \ll 1$. To leading orders in y and ϵ , equation (2.1) is transformed into

$$\tilde{R}_0^2 \ddot{y} = -\omega_e^2 \frac{R_0^5}{\tilde{R}_0^3} y + \frac{P_0}{\rho_l} \left(\frac{R_0^3}{\tilde{R}_0^3} - (1 - p \cos \omega_e \tau) \right) \quad (4.13)$$

Requiring the slowly varying (secular) term on the right-hand side to vanish, we have to choose

$$\tilde{R}_0(\tau) = R_0 / (1 - p \cos(\omega_e \tau))^{1/3} = R_0 / (1 - p \cos(\omega t))^{1/3}. \quad (4.14)$$

With this definition, (4.13) results in a Hill equation:

$$\ddot{y} + \omega_e^2 (1 - p \cos \omega t)^{5/3} y = 0. \quad (4.15)$$

Because of the separation of time scales $\omega_e \gg \omega$ this equation represents a harmonic oscillator with slowly varying eigenfrequency, i.e., the afterbounce frequency $\omega_{ab} = \omega_e (1 - p \cos \omega t)^{5/6}$. For this system, $E(\omega_{ab})/\omega_{ab}$ (with $E = \langle y^2 \rangle \omega_{ab}^2/2$ being the oscillator energy) is an adiabatic invariant (see Hinch 1991), i.e.,

$$\langle y^2 \rangle (1 - p \cos \omega t)^{5/6} = \text{const.}, \quad (4.16)$$

where the mean $\langle \cdot \rangle$ is an average over the fast time scale. Note that in the time interval $\pi/2 \lesssim \omega t \lesssim 3\pi/2$ of afterbounces $(1 - p \cos \omega t) > 0$. It follows that the amplitude of the afterbounces changes as $\tilde{R}_0 y \propto (1 - p \cos \omega t)^{-3/4}$.

The resonance structure of (4.15) still cannot be evaluated analytically. Yet the parametric driving of (4.15) has a very similar shape to the cosine driving of a Mathieu equation. We can therefore further approximate (4.15) by choosing suitable constants Q_1, Q_2 , where we require

$$Q_1 - Q_2 \cos(\omega t) = (1 - p \cos(\omega t))^{5/3} \quad \text{for } \omega t = \frac{\pi}{2}, \pi, \quad (4.17)$$

i.e., $Q_1 = 1$, $Q_2 = (1 + p)^{5/3} - 1$. The errors in this approximation are only a few percent in the time interval $\sim [\pi/2, 3\pi/2]$ of afterbounces we focus on. As an analytically accessible approximation to the afterbounce dynamics of (2.1) we have thus the Mathieu equation

$$y'' + 4 \frac{\omega_e^2}{\omega^2} \left(1 - \left[(1 + p)^{5/3} - 1 \right] \cos 2\hat{x} \right) y = 0 \quad (4.18)$$

with dimensionless time $\hat{x} = \omega t/2$; the primes denote derivatives with respect to \hat{x} .

The contribution of surface tension may be included if $\alpha_s \ll 1$ to yield a refinement of (4.18):

$$y'' + 4 \frac{\omega_e^2}{\omega^2} \left(\left(1 + \frac{2}{3} \alpha_s \right) - \left[(1 + p)^{5/3} - 1 + \frac{2}{3} \alpha_s \left(1 + 2p - (1 + p)^{5/3} \right) \right] \cos 2\hat{x} \right) y = 0, \quad (4.19)$$

with the factor α_s from (2.6). Note that a simple substitution $\omega_e \rightarrow \omega_s$ does not cover all first-order effects of α_s .

For certain parameter combinations, equation (4.19) shows parametrically stable or unstable solutions. Because $\omega_e/\omega \gg 1$, the best analytical approximation to these characteristic values is given by the asymptotic series (Abramowitz & Stegun 1972)

$$b = \nu\sqrt{s} - \frac{\nu^2 + 1}{8} - \frac{\nu^3 + 3\nu}{2^6\sqrt{s}} \mp \dots \quad (4.20)$$

with $b = 4\frac{\omega_e^2}{\omega^2}[(1-2\alpha_s/3)(1+p)^{5/3} + 4\alpha_s/3 \cdot (1+p)]$, $s = 8\frac{\omega_e^2}{\omega^2}[(1-2\alpha_s/3)(1+p)^{5/3} + 4\alpha_s/3 \cdot p - 1 + 2\alpha_s/3]$, and $\nu = 2k_M \pm 1$, where the sign distinguishes even from odd Mathieu solutions. k_M is the order of the Mathieu resonance, corresponding to the number of afterbounces in the RP equation (see below). We take here only the leading term on the right-hand side of (4.20) and treat the case $k_M \gg 1$, so that $\nu \approx 2k_M$; moreover, we only keep terms up to first order in α_s . This yields ambient radii $R_0^{(k_M)}$ for which the oscillation shows maximum stability against parametric excitation:

$$\begin{aligned} R_0^{(k_M)} &= \left(\frac{3P_0}{2\rho_l\omega^2}\right)^{1/2} \frac{q^{5/3}}{\sqrt{q^{5/3}-1}} \frac{1}{k_M} + \frac{2\sigma}{3P_0} \left(\frac{q^{5/3}-2q+1}{q^{5/3}-1} + 2\frac{2-q^{2/3}}{q^{2/3}}\right) \\ &\approx 74.0 \mu\text{m} \cdot \frac{q^{5/3}}{\sqrt{q^{5/3}-1}} \frac{1}{k_M} + 0.487 \mu\text{m} \cdot \left(\frac{q^{5/3}-2q+1}{q^{5/3}-1} + 2\frac{2-q^{2/3}}{q^{2/3}}\right) \end{aligned} \quad (4.21)$$

Here we have abbreviated $q = (p+1)$. Note that the correction term due to surface tension does not depend on k_M .

Although the behaviour of the RP oscillator is fairly well described by Mathieu oscillations in the afterbounce phase (see e.g. figure 13), it is of course entirely different during the expansion interval of the cycle. Therefore, some information about the overall shape of the oscillation must enter into our analysis. Especially, Mathieu solutions can be T - or $2T$ -periodic. RP dynamics in the SL regime, however, only allows for T -periodic solutions, as the $2T$ -periodic Mathieu solutions would require large negative values for y . Therefore, every second resonance of (4.19) must be dropped, i.e., the resonance of order k_M of (4.19) corresponds to resonance number $k = k_M/2$ of (2.1), so that the k^{th} resonance radius $R_0^{(k)}$ of (4.19) for a dynamics with k afterbounces is obtained by replacing k_M by $2k$.

We must also provide additional information about the length of the afterbounce interval. Figure 13 shows that this length, which is almost independent of p for our Mathieu approximation, is significantly reduced for increasing p in the case of the RP equation, as the expansion interval lasts longer. This is a property of the nonlinear part of the RP cycle (cf. the next subsection), which cannot be modelled within the Mathieu approximation. In the Appendix it is shown that the length of the afterbounce phase (and therefore the resonance number k) has to be rescaled according to $k \rightarrow C(p) \times k$ with $C(p)$ approximately given by the expansion $C(p) \approx 0.688 - 0.548(p - \pi/2) + 0.418(p - \pi/2)^2$ (cf. (B 2)).

Figure 14 presents a comparison of the computed resonance radii of order (number of afterbounces) k from numerical solutions of (2.1) – both for relative maxima and minima of $R_{max}(R_0)$ – and from (4.19) for driving pressure amplitudes $p = 1.2$ and 1.5 , corrected

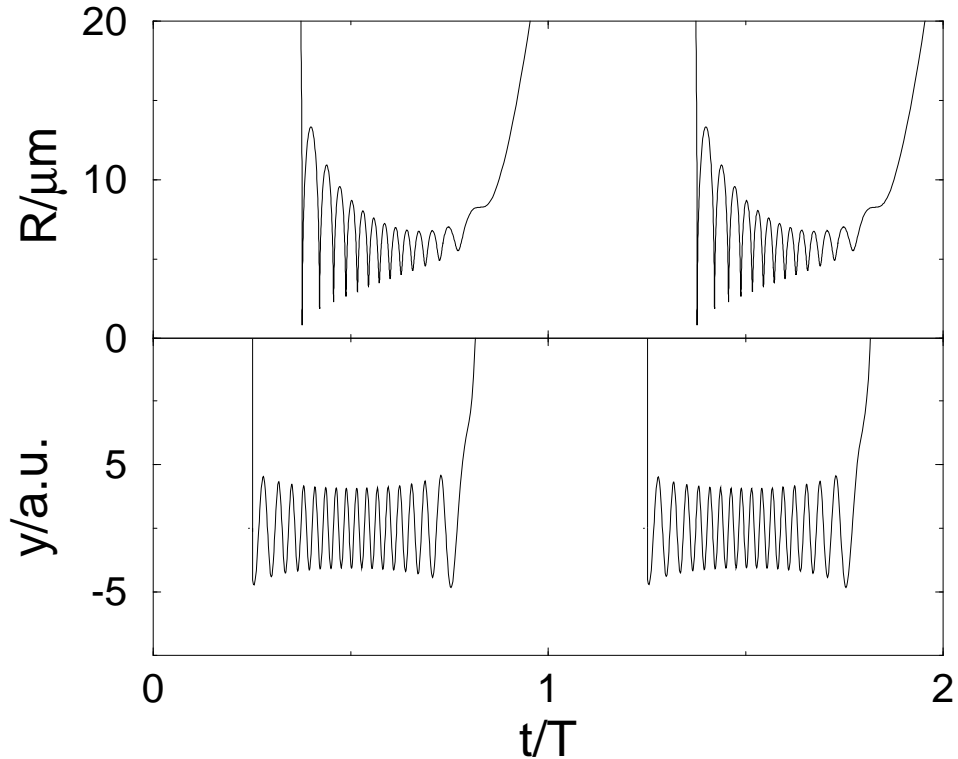


FIGURE 13. Comparison of time series from the numerical solution of the RP equation (2.1) (upper) and a T -periodic solution of the Mathieu approximation (4.19) (lower) for the same parameters $p = 1.5$, $R_0 = 6.0 \mu\text{m}$. The onset of afterbounces is delayed in the full RP dynamics. The correction factor (B 2) has to be employed. As the Mathieu solution is divergent (grows exponentially from cycle to cycle), the lower curve was normalized once per cycle.

with $C(p)$. The resonance locations are in good agreement for both pressures, considering the multitude of approximations they were calculated with.

In the stability maxima marked by $R_0^{(k)}$ the bubble is less excitable by the driving than bubbles with neighboring R_0 . Therefore the expansion ratio has a local minimum and the average pressure $\langle p_{\text{gas}} \rangle_4 \propto 1/R_{\text{max}}^3$ experiences a local maximum. The existence of such wiggles in R_{max}/R_0 (and therefore in $\langle p_{\text{gas}} \rangle_4$) leads to the possibility of multiple equilibria for given experimental parameters P_a and p_∞ : the ambient radius can adjust itself diffusively to different stable equilibrium values, depending on initial conditions and/or perturbations. For an analysis of the physical consequences of multiple equilibria we refer the reader to the work of Brenner *et al.* (1996a), Hilgenfeldt *et al.* (1996) and Crum & Cordry (1994).

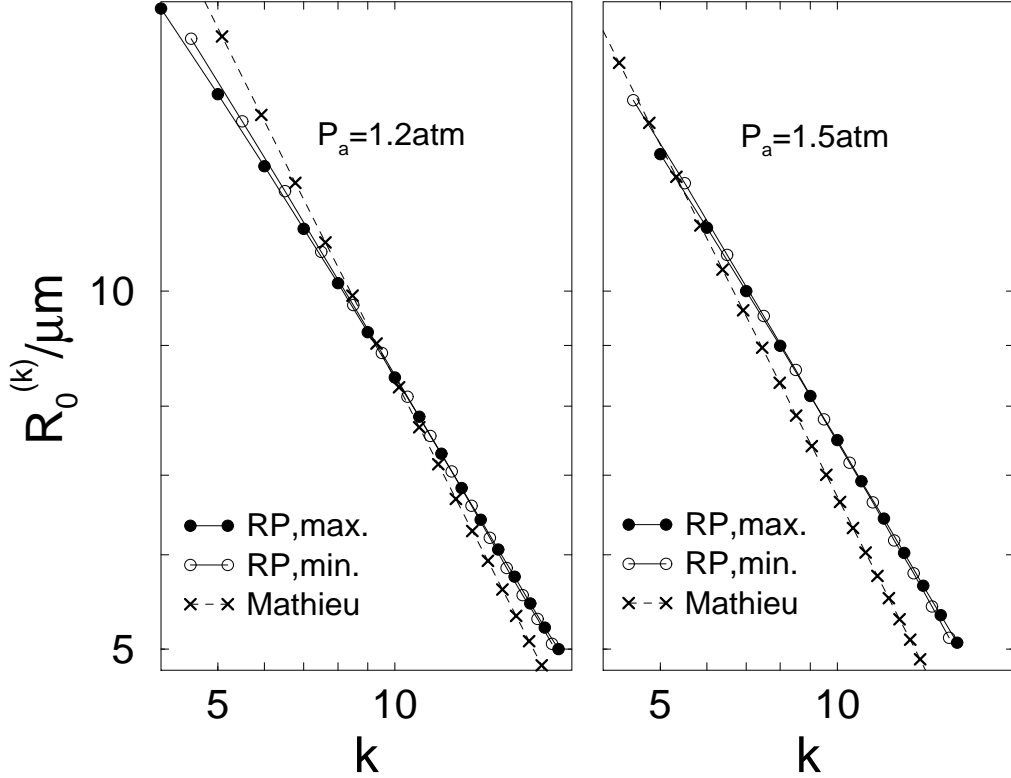


FIGURE 14. Ambient radii $R_0^{(k)}$ as a function of resonance order $k = k_M/2$ from the full solution of (2.1) (circles) and the analytical Mathieu approximation (4.21) (crosses); $P_a = 1.2 \text{ atm}$ (left) and 1.5 atm (right). Note that the circles represent relative maxima *and* minima of R_{max} , because the Mathieu equation admits twice as many resonance values as the RP equation. The Mathieu solutions were rescaled by the factor $C(p)$ of equation (B 2).

4.4. Bubble Expansion (regions E_1 , E_2)

We wish to be more quantitative about the properties of the expansion phase now. Despite the small portion of parameter space for SL bubbles, there are different types of expansion behaviour to be identified depending on p and R_0 . For $p \gtrsim 1$ and large $R_0 \gtrsim 10 \mu\text{m}$, the gas pressure plays an important role and balances the dynamical pressure, which is dominated by p_{vel} for most of the cycle, so that a first approximation to the dynamics is:

$$\rho_l \frac{3}{2} \dot{R}^2 = p_{gas}(R, t) \quad (4.22)$$

With $p_{gas}(R, t) \approx P_0 R_0^3 / R^3$ for large R_0 , this equation yields a solution for $R(t)$:

$$R(t) = \left[R_{-}^{5/2} + \frac{5}{2} \left(\frac{2P_0}{3\rho_l} \right)^{1/2} R_0^{3/2} (t - t_{-}) \right]^{2/5} \quad (4.23)$$

with the starting time of expansion t_- and starting radius $R_- = R(t_-)$. For radii $R \gg R_-$, (4.23) reduces to a Rayleigh-type expansion law, which gives a scaling relation for the maximum radius:

$$R_{max} \propto R_0^{3/5} \quad (4.24)$$

if we assume that the length of the expansion interval is independent of R_0 , which is a good assumption except for small R_0 below the Blake threshold (3.4). The law (4.24) can numerically be confirmed for large R_0 , see Hilgenfeldt *et al.* (1996). Together with (2.11) this yields $\langle p_{gas} \rangle_4 \propto R_0^{6/5}$.

For higher driving pressure amplitudes or smaller R_0 , i.e., in most of the SL parameter region, the approximation (4.22) is too crude. Instead, one has to take into account the balance of the dynamical pressures p_{acc}, p_{vel} and the external pressure p_{ext}

$$\rho_l \left(R \ddot{R} + \frac{3}{2} \dot{R}^2 \right) = P_0(p \cos \omega t - 1), \quad (4.25)$$

as can be seen e.g. in figure 15.

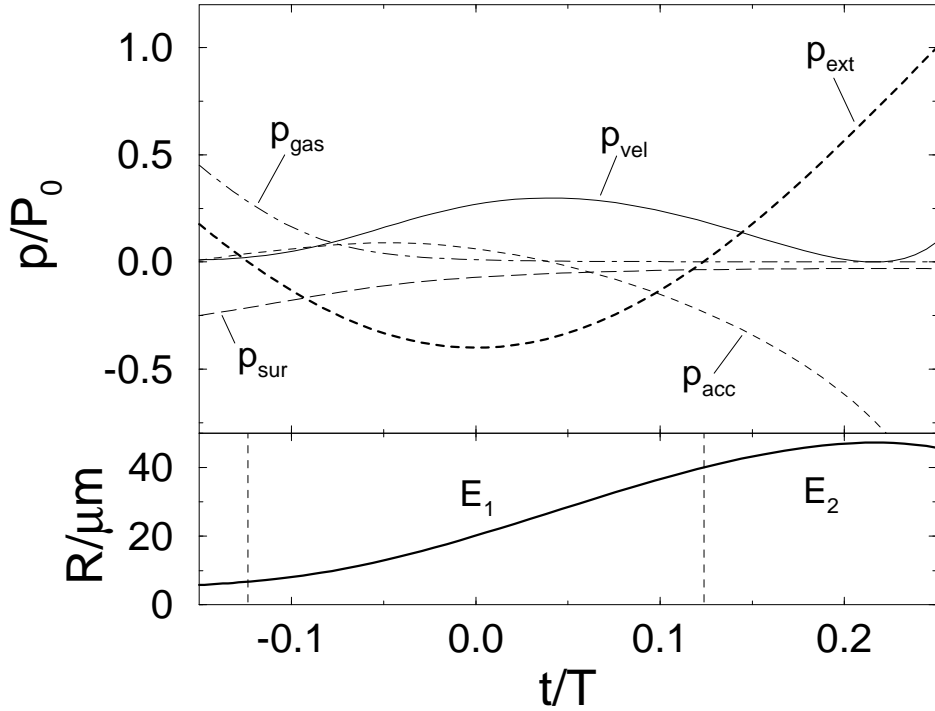


FIGURE 15. Upper: important pressure contributions for $P_a = 1.4 \text{ atm}$, $R_0 = 4.0 \mu\text{m}$ during the expansion phase. The thick dashed line gives the external pressure $p_{ext} = P_0 - P_a \cos \omega t$. In the time interval E_1 , it is primarily balanced by p_{vel} (solid), in E_2 by p_{acc} (dashed). Lower: bubble radius expansion dynamics for the same parameters.

In the work of Löfstedt *et al.* (1993), the left-hand side of (4.25) has been approximated using a power series for $R(t)$. This leads to a bubble expansion which is linear in time, with a velocity proportional to $\sqrt{p-1}$. The first nonlinear corrections are of fourth order in t .

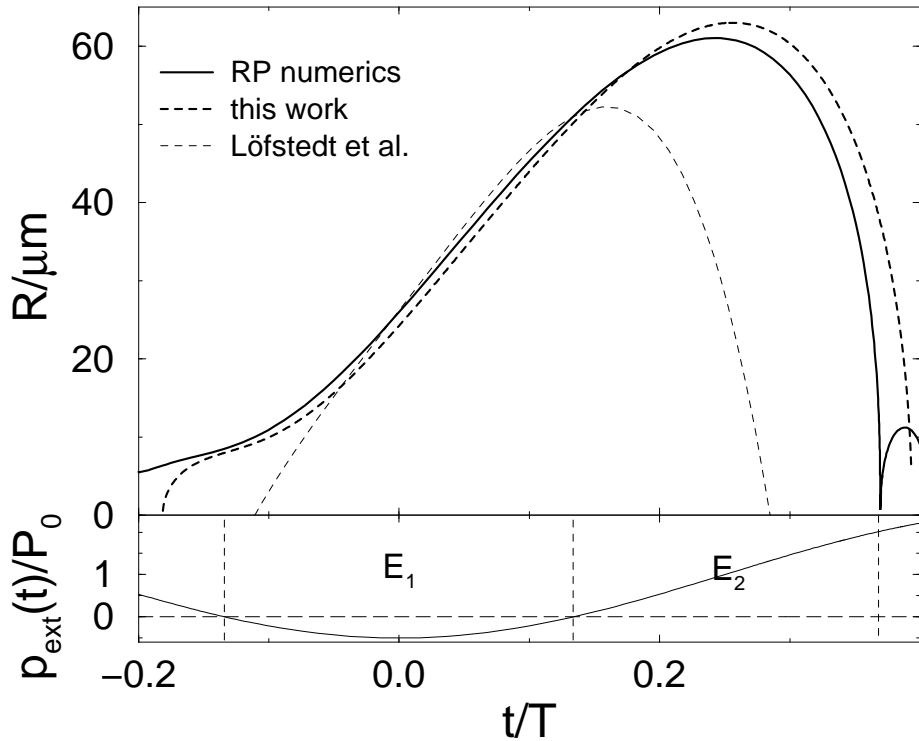


FIGURE 16. Comparison of RP dynamics (solid) and theoretical approximation (dashed) of bubble expansion dynamics for $P_a = 1.5 \text{ atm}$, $R_0 = 5.0 \mu\text{m}$. The theoretical solution becomes complex left and right of its zeros. Also shown is the suggested theoretical solution (thin dashed line) from equation (29) of Löfstedt *et al.* (1993), where $R(t = 0)$ was matched to the value of the RP dynamics.

However, an expansion like this turns out to be a series which is not well-controlled. Especially, no reliable values for the time t_{max} and value R_{max} of the maximal radius can be derived (cf. figure 16). We therefore follow a different ansatz: consider the dynamical terms p_{acc} and p_{vel} for a typical bubble expansion (figure 15). During the first, almost linear part $|p_{vel}| \gg |p_{acc}|$, whereas when the maximum is approached and the bubble decelerates, $|p_{acc}| \gg |p_{vel}|$. This suggests a division of the expansion interval into two parts (denoted by E_1 and E_2 in figures 2(b), 15, and 16). Observing that the combination $R\ddot{R} + \dot{R}^2$ is just the second derivative of $R^2/2$, (4.25) can be approximated with good

accuracy by

$$\frac{d^2}{dx^2} R^2 = \frac{4}{9} R_{res}^2 (p \cos x - 1) + \mathcal{O} \left(R \frac{d^2}{dx^2} R \right) \quad \text{for } x_- \leq x \leq x_+, \quad (4.26a)$$

$$\frac{d^2}{dx^2} R^2 = \frac{2}{3} R_{res}^2 (p \cos x - 1) + \mathcal{O} \left(\left(\frac{d}{dx} R \right)^2 \right) \quad \text{for } x_+ \leq x \leq x_m. \quad (4.26b)$$

Here we have introduced the dimensionless time $x \equiv \omega t$ and the linear bubble resonance radius R_{res} from (2.7); x_m is given by $R(x_m) = R_{max}$. The rational prefactors on the right-hand side make sure that the dominant terms p_{vel} in (4.26a) and p_{acc} in (4.26b) are correctly represented, while the other terms gives contributions of the indicated order in each case. The starting time $x_- = x_-(p)$ and the transition time $x_+ = x_+(p)$ between both solutions are given by the zeros of p_{ext} , i.e., $x_+(p) = -x_-(p) = \arccos 1/p$. Equations (4.26a, b) can be integrated analytically requiring continuity and differentiability at x_+ for the overall solution. To complete the problem, initial conditions at x_- have to be imposed: we set $R_- = R(x_-) = \zeta R_0$ with a parameter $\zeta \sim 1$ whose value is not crucial for the shape of the solution. An estimate of ζ can be computed from algebraic equations, but not in an explicit form. ζ lies between 1.2 and 2.0 for typical R_0 of SL bubbles; for simplicity, we choose $\zeta = 1.6$ in all calculations. For the initial velocity, we observe that x_- marks the transition from the afterbounce regime, where the bubble essentially oscillates with its eigenfrequency, to the expansion regime, where the governing time scale is the driving period T . Therefore, we set $R'_- = (dR/dx)(x_-) = R_-$, corresponding to $\dot{R}_- = \omega R_-$ in dimensional terms.

Figure 16 shows that the shape of the expansion as well as time and value of the maximum are reproduced satisfactorily. From the solutions of (4.26a) in E_1 and (4.26b) in E_2 one obtains a system of equations for R_{max} and x_m :

$$R_{max}^2 = R_-^2 (1 + 2(x_m + x_+)) + \frac{2}{3} R_{res}^2 \left[1 - p \cos x_m - \frac{1}{2}(x_m^2 - x_+^2) + \frac{1}{3}(p \sin x_+ - x_+)(x_m + 3x_+) \right], \quad (4.27)$$

$$p \sin x_m - x_m + \frac{1}{3}(p \sin x_+ - x_+) + \frac{3R_-^2}{R_{res}^2} = 0. \quad (4.28)$$

Note that (4.27), (4.28) give the position and height of the radius maximum *without* any freely adjustable parameters. The inset of figure 17 shows the maximum radii obtained with these formulas for $R_0 = 5 \mu\text{m}$ and $9 \mu\text{m}$ and $p = 1 - 5$ together with results from a complete RP computation. Apart from the resonance wiggles (cf. Section 4.3), the curves are very well reproduced both within the p regime for SL bubbles and for the much higher pressure amplitudes of cavitation field experiments.

Equation (4.28) is transcendental, and R_{max} and x_m do not have simple analytical representations. One can, however, derive simple expressions in several limiting cases: if $p \gg 1$, we obtain after a lengthy calculation

$$R_{max} \approx \sqrt{2/3} R_{res} (Fp - G)^{1/2} \quad (4.29)$$

with constants $F = 1 + 5\pi/6 = 3.618 \dots$, $G = 19\pi^2/24 - 1 = 6.813 \dots$. This formula is a

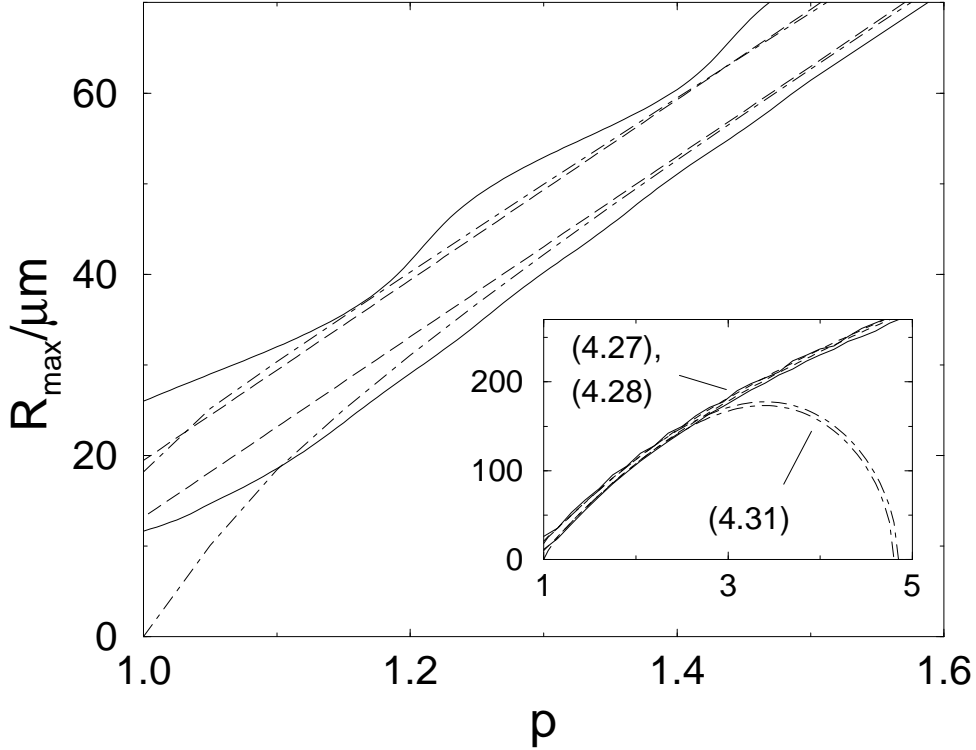


FIGURE 17. Comparison of direct numerical results of R_{max} (solid) for $R_0 = 5 \mu\text{m}$ (lower) and $R_0 = 9 \mu\text{m}$ (upper) in the p range relevant for SL with the approximate law (4.31) (dot-dashed) and the simpler formula (4.32) (long dashed). The inset shows that the full theory (dashed) according to (4.27), (4.28) for $R_{max}(p)$ for the same two R_0 gives excellent agreement with the direct RP computation (solid) for both the SL range and the cavitation field regime $p \sim 2 - 5$. Even the approximation (4.31) yields good results up to $p \sim 3$ (dot-dashed).

good approximation only if $p \gtrsim 5$. For $p \gtrsim 1$, i.e., the case of interest for sonoluminescent bubbles, we can expand x_m around $x = \pi/2$. Moreover, as $R_{res} \gg R_0$ for SL driving frequencies, we can also neglect the last term on the right-hand side of (4.28). To leading order in $(x_m - \pi/2)$, (4.28) then becomes

$$x_m = p + \frac{1}{3}(p \sin x_+ - x_+); \quad (4.30)$$

remember that $x_+ = x_+(p) = \arccos(1/p)$. For $p \in [1.0, 1.5]$, the second term of the right-hand side of this equation is never greater than $0.185p$ in absolute magnitude, so that $x_m = p$ is a good approximation. Inserting into (4.27) gives

$$R_{max}^2 = f(p)R_0^2 + g(p)R_{res}^2 \quad \text{with} \quad (4.31a)$$

$$f(p) = \zeta^2 (1 + 2(p + x_+)), \quad (4.31b)$$

$$g(p) = \frac{2}{3} \left[1 - p \cos p - \frac{1}{2}(p^2 - x_+^2) + \frac{1}{3}(p \sin x_+ - x_+)(p + 3x_+) \right]. \quad (4.31c)$$

The second term in (4.31a) is much greater than the first; thus, it is *not* primarily R_0 which determines R_{max} , but the resonance radius R_{res} . With $R_{res} \propto 1/\omega$, we see that the expansion ratio is (at constant p and R_0) roughly inversely proportional to the driving frequency, i.e., upscaling of SL collapses can be achieved by lowering ω , which was also seen in experiment by R. E. Apfel (private communication, 1996). In the same way, a higher ambient pressure P_0 (while keeping $p = P_a/P_0$ constant) will lead to higher expansion ratios because of the dependence of R_{res} on P_0 (see (2.7)). A further simplification of (4.31) can be obtained from a stringent expansion in $(p - \pi/2)$ and R_0 , which yields to leading order the simple result

$$\frac{R_{max}}{\mu m} = 67.2 + 0.112 \left(\frac{R_0}{\mu m} \right)^2 + 99.5(p - \pi/2) + \mathcal{O}((p - \pi/2)^2). \quad (4.32)$$

Figure 17 shows the very good agreement of (4.31) and (4.32) with full RP dynamics for several R_0 over the whole range of pressures in SL experiments. The approximation breaks down only at $p \sim 3$, where $x_m \approx p$ is no longer valid, see inset of figure 17. The expansion ratio is also accurately reproduced for moderate or large R_0 by this formula, as seen in figure 18. The deviations for small R_0 are due to neglecting p_{sur} , which becomes the dominant influence as R_0 approaches R_0^{tr} .

One would therefore like to include the effects of surface tension into (4.31). We make the following ansatz: instead of (4.26a, b), we write

$$\frac{d^2}{dx^2} R^2 = \frac{4}{9} R_{res}^2 \left(p \cos x - \left(1 + \frac{\alpha_s}{K(p)} \right) \right) \quad \text{for } x_- \leq x \leq x_+, \quad (4.33a)$$

$$\frac{d^2}{dx^2} R^2 = \frac{2}{3} R_{res}^2 \left(p \cos x - \left(1 + \frac{\alpha_s}{K(p)} \right) \right) \quad \text{for } x_+ \leq x \leq x_m. \quad (4.33b)$$

This models the influence of p_{sur} by an average pressure contribution of $P_0 \alpha_s / K(p)$, where K is taken to be independent of R_0 . Expanding x_m again around $\pi/2$, we get

$$R_{max}^2 = f(p) R_0^2 + \left[g(p) + \frac{2}{3} \frac{\alpha_s}{K(p)} \left(\frac{1}{2}(p^2 + x_+^2) + \frac{1}{3}px_+ \right) \right] R_{res}^2 \quad (4.34)$$

with $f(p)$, $g(p)$ from (4.31b, c). With this expression, $(R_{max}/R_0)(R_0)$ shows a global maximum at

$$R_0^c(p) = \frac{3\sigma}{P_0 K(p)} \frac{\frac{1}{2}(p^2 + x_+^2) + \frac{1}{3}px_+}{g(p)} \quad (4.35)$$

For large enough p , we can equate (4.35) and (3.5), because R_0^{tr} and R_0^c are very close then. This gives an estimate for $K(p)$:

$$K(p) = \frac{9}{4} \sqrt{3} (p-1) \frac{\frac{1}{2}(p^2 + x_+^2) + \frac{1}{3}px_+}{g(p)} \quad (4.36)$$

In the regime of SL driving pressures ($p = 1.2 \dots 1.5$) $K(p)$ depends only weakly on p ; its value lies between 7.5 and 9.4. The ansatz (4.33a, b) proves very successful for the description of $(R_{max}/R_0)(R_0)$ over the whole range of relevant R_0 , as can be seen from figure 18.

From (4.34), we obtain expansion ratios and, using (2.9) and (2.11) for given gas

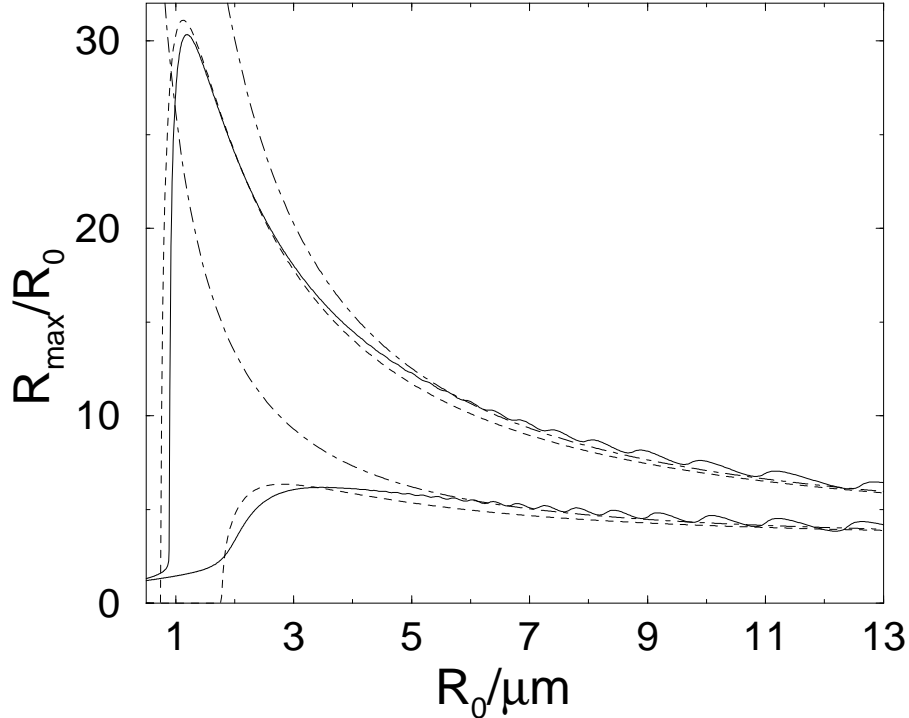


FIGURE 18. Direct numerical computation (solid) and theory (dot-dashed) according to (4.31) for the expansion ratio $(R_{max}/R_0)(R_0)$ at $p = 1.2$ (lower) and 1.5 (upper). The dashed curve from (4.34) takes surface tension into account and is able to reproduce the numerical graphs for almost all R_0 .

concentration p_∞/P_0 , an approximation for the location $R_0(p)$ of diffusive equilibria can be computed. Figure 19 shows that both the stable and the unstable branches of the equilibrium curves (taken from figure 1) are reproduced satisfactorily for both high and low gas concentrations.

When, starting on the stable branch, p is lowered, R_{max}/R_0 becomes smaller and, by (2.11), $\langle p_{gas} \rangle_4$ becomes larger. The corresponding equilibrium ambient radii R_0 shrink. Eventually, the minimum of $\langle p_{gas} \rangle_4/P_0$ becomes larger than p_∞/P_0 (see figure 3) and no R_0 can fulfill the equilibrium condition. This situation corresponds to the turning point of the diffusive equilibria in figure 1 and figure 19.

5. Role of surface tension and liquid viscosity

The previous sections have provided a detailed analysis of the dynamics of SL bubbles. How will these results change if we introduce a different fluid with different surface tension σ and/or fluid viscosity η_l ?

Surface tension is the crucial parameter for the location of the Blake threshold in

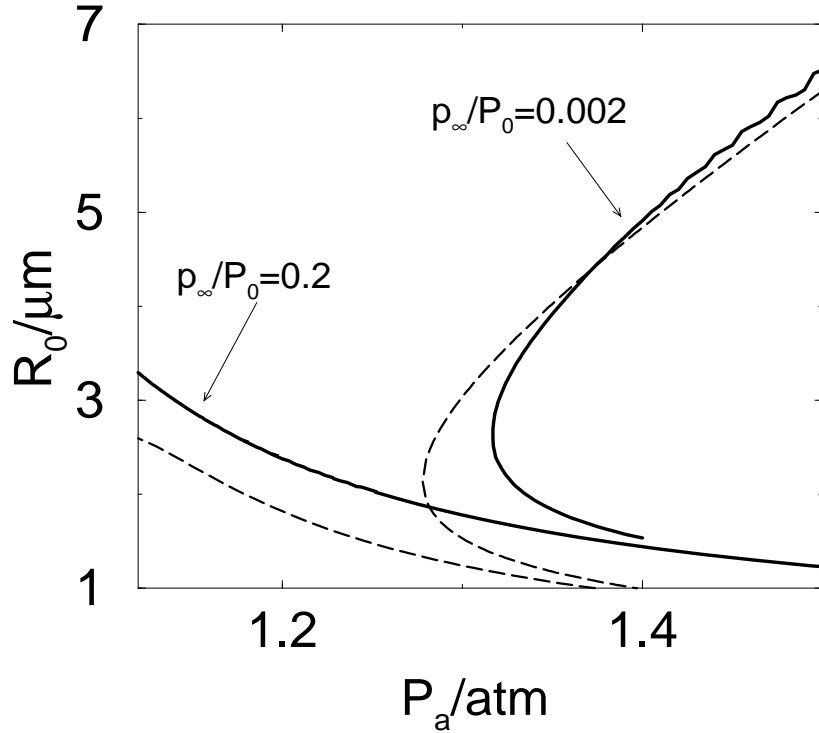


FIGURE 19. Diffusive equilibrium lines from figure 1 (solid) and their approximation using (4.34) (dashed) near the parameter domain of sonoluminescing bubbles.

parameter space (cf. also Löfstedt *et al.* 1995 or Akhatov *et al.* 1997). The transition from weakly oscillating to strongly collapsing bubbles and therefore the boundary of the SL region determined by (1.1) is entirely controlled by σ . If we had $\sigma \rightarrow 0$, bubbles with any R_0 would be strongly collapsing, i.e., liquids with small surface tension should allow for violent collapses at smaller P_a . On the other hand, in liquids with high σ larger P_a and R_0 are required for collapses. Although a larger σ has a stabilizing effect on the bubble surface, (3.5) and (4.35) show that the $|M_g| = 1$ line overtakes the shape instability threshold in P_a - R_0 parameter space (cf. Hilgenfeldt *et al.* 1996), so that no stable SL should be possible if σ is e.g. five times higher than in water. This is easily confirmed by the numerical solution of the RP equation, see figure 20(a).

At first sight it seems that fluid viscosity could have been neglected in (2.1) right from the start. Apart from a slight damping effect during the afterbounce phase, the influence of η_l for water on bubble dynamics is hardly noticeable, even a tenfold increase of η_l only reduces the maximum radius by $\approx 10\%$ (figure 21a,b). We can, however, estimate by how much the viscosity would have to be enhanced to have a significant effect: the damping of a high viscosity liquid should ultimately prevent the bubble from collapsing violently and therefore it will never fulfill the energy transfer condition (1.1). As the collapse is

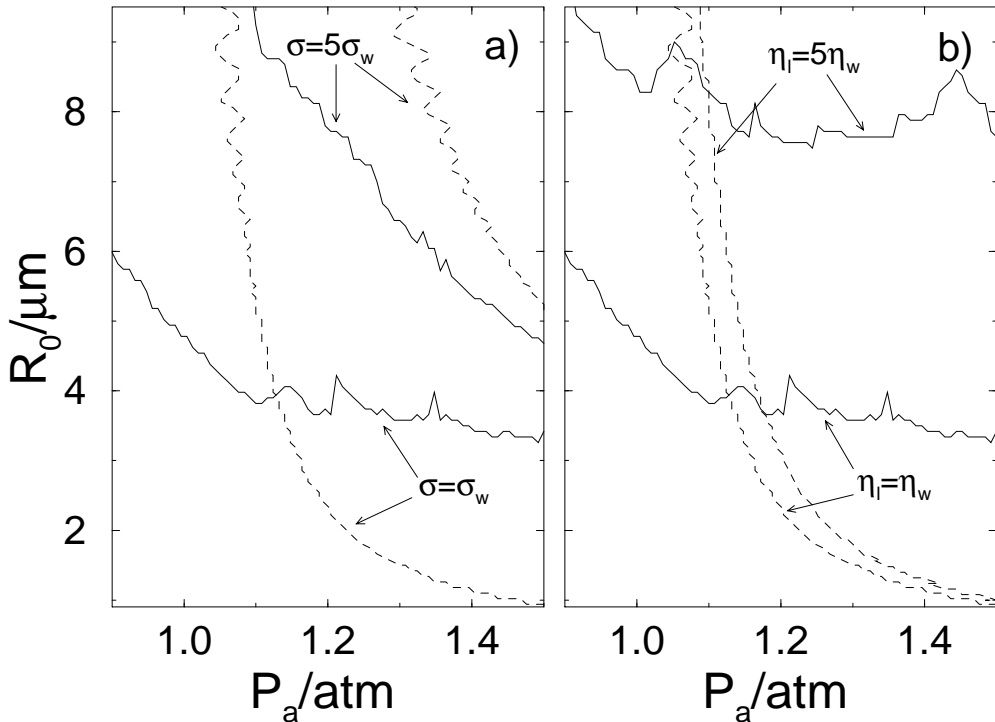


FIGURE 20. Parametric stability thresholds (solid), calculated as elaborated in Hilgenfeldt *et al.* (1996), and $|M_g| = 1$ lines (dashed) for bubbles of different surface tension (a) and viscosity (b). All other parameters were fixed at the values for water. Increasing σ makes the region of potential SL bubbles above the $|M_g| = 1$ and below the stability threshold vanish, whereas higher η_l enlarges this area.

in fact the first afterbounce minimum, an estimate for this critical η_l^c can be obtained if we demand the afterbounces to be overdamped. The viscosity η_l introduces a damping term in the linearization of the RP equation (2.4). It is easy to see that overdamped motion requires

$$\frac{2\eta_l^c}{\rho_l R_0^2} \gtrsim \omega_e \left(1 + \frac{\alpha_s}{3}\right). \quad (5.1)$$

With the definition of ω_e , it follows

$$\eta_l^c \gtrsim \left(1 + \frac{\alpha_s}{3}\right) \left(\frac{3}{4} \rho_l P_0 R_0^2\right)^{1/2}. \quad (5.2)$$

With a typical value $R_0 = 4\mu\text{m}$ and keeping σ , ρ_l at the values for water, we obtain that $\eta_l^c \gtrsim 40\eta_{\text{water}}$. This is confirmed by direct computation of (2.1) using η_l^c and strong driving pressure $P_a = 1.4\text{ atm}$, see figure 21(c)-(e). Viscosities in this range can be easily achieved in mixtures of water and glycerine. For moderate glycerine percentage, the viscosity is not very different from pure water, but for high glycerine contents it

rises dramatically. The required factor of 40 is (at 10°C) reached for $\approx 70\%$ glycerine (weight percentage). Above this percentage, it would be extremely difficult to obtain collapses strong enough to ensure energy transfer and the ignition of SL. Moreover, chemical dissociation reactions in air cannot take place, which seem to be necessary for SL stability using air at moderate degassing levels (Lohse *et al.* 1997). This may be the reason why Gaitan (1990) was not able to observe stable bubbles above a glycerine percentage of $\approx 60\%$. The actual threshold for SL should occur at slightly smaller η_l than predicted by (5.2), because even if the collapse minimum is not completely damped out, the collapse is already considerably weakened (figure 21c). Also, the threshold should be higher because of the additional damping effect of thermal dissipation (see Vuong & Szeri 1996, Yasui 1995) which is not included in our approach.

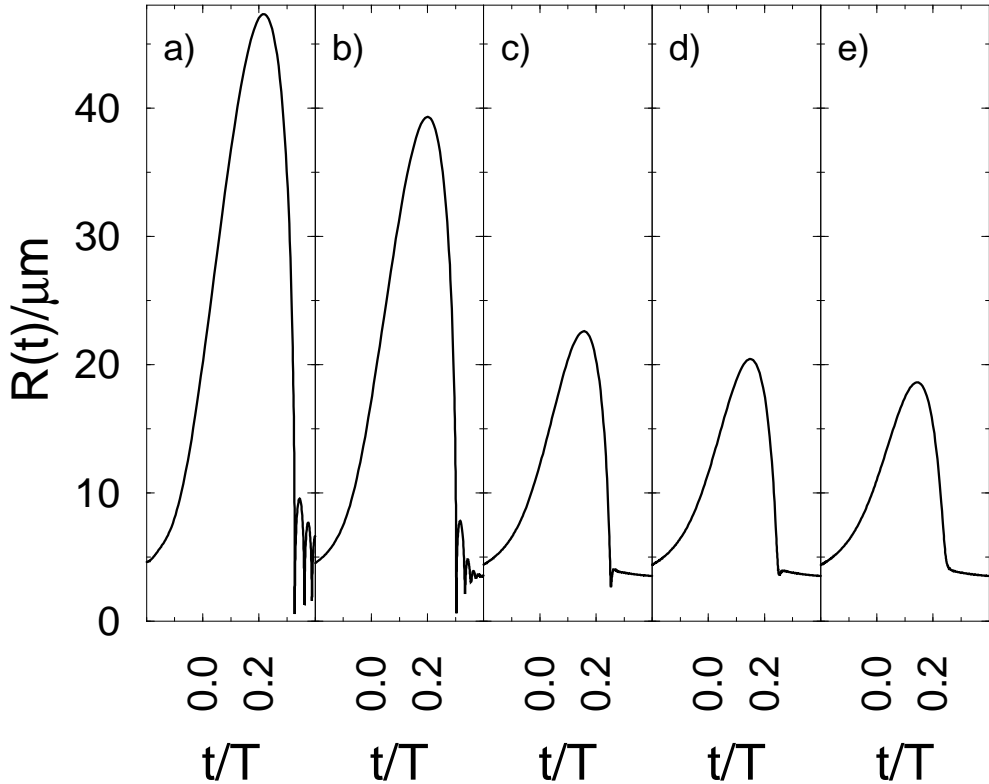


FIGURE 21. Bubble dynamics $R(t)$ for different viscosities $\eta_l/\eta_{water} = 1(a)$, $10(b)$, $35(c)$, $40(d)$, $45(e)$. $R_0 = 4\ \mu\text{m}$ and $P_a = 1.4\ \text{atm}$ in all cases. The transition from collapse/afterbounce behaviour to aperiodic dynamics occurs near $\eta_l/\eta_{water} = 40$, as predicted from (5.2).

Even for smaller $\eta_l \sim \eta_{water}$, fluid viscosity is an important contribution to the damping of bubble surface oscillations, as was shown in Hilgenfeldt *et al.* (1996). Therefore, a moderate increase in η_l does not lead to significant changes in the $R(t)$ dynamics itself (and therefore in the $|M_g| = 1$ curve), but it helps to stabilize bubbles at larger R_0 .

This change affects only the parametric and afterbounce instabilities (see Hilgenfeldt *et al.* 1996), which can show accumulation effects over several driving periods, but not the Rayleigh-Taylor instability, which is directly dependent on the acceleration of the bubble wall and cannot change significantly when the $R(t)$ dynamics does not. Therefore, the Rayleigh-Taylor process still cuts off the bubble stability region (cf. figure 6 of Hilgenfeldt *et al.* 1996) at $P_a \approx 1.45\text{atm}$ almost independent of viscosity, whereas at smaller P_a , much larger bubbles can be stable if η_l is enhanced.

In figure 20(b), we show surface stability curves for different fluid viscosities. For high η_l , the region of stably sonoluminescing bubbles between the almost unaffected $|M_g| = 1$ curve and the increased stability threshold is considerably enlarged. This would probably correspond to a substantial upscaling of SL intensity. Gaitan's (1990) experimental observation that a moderate percentage of glycerine helps to establish stable SL bubbles supports this conjecture (see also the experimental results of Gaitan *et al.* 1996 for fluids of different viscosity and surface tension). Combining our results for σ and η_l , we conclude that the ideal fluid for violently collapsing, but surface stable bubbles should have small surface tension and high viscosity.

6. Conclusions

The analysis of the RP equation presented here has explained quantitatively quite a lot of features seen in numerical computations of RP dynamics. One cycle of oscillation of this highly nonlinear system can be completely divided into subsections in which its behaviour can be accurately approximated by analytically integrable equations. While being in the spirit of Löfstedt *et al.*'s (1993) previous analysis, the present work presents more complete and more detailed results. We emphasize that there are no freely adjustable parameters in our approach.

We made use of these approximations to calculate analytical laws for the bubble's collapse, afterbounce behaviour, expansion dynamics, maximum radius, and expansion ratio. With these results we could clarify parameter dependences of numerically calculated curves of diffusive equilibria in P_a - R_0 parameter space as those in figure 1. A summary of relevant analytical relations and predictions for experimental verification was already given in the Introduction.

An approximation of the RP equation by a Mathieu equation has explained the wiggly resonance structure characteristic for many quantities derived from RP dynamics. The concept of a quasistatic Blake threshold between regimes of weakly oscillating and strongly collapsing bubbles was able to shed light on the existence of *stable* diffusive equilibria in the SL regime for high driving pressures. The change of sign in the slope of $\langle p_{\text{gas}} \rangle_4(R_0)$ is a generic feature of RP dynamics, resulting from the dominance of surface tension pressure at small R_0 . This allows the bubble to reach a stable diffusive equilibrium.

In all approximations of the RP equation, the fluid viscosity term for water or similar liquids could be neglected without causing large errors. Both numerical computations and

analytical estimates of the magnitude of p_{vis} show that η_l has to be as high as $\sim 40 \eta_{water}$ to become a dominant contribution to bubble dynamics. Viscosity does, however, have a strong influence on the dynamics of surface oscillations; parametric instabilities are weakened for larger η_l .

Surface tension is the underlying cause for the change from unstable to stable diffusive equilibria, which stabilizes small bubbles to an extent that they can only show weak oscillations. For fluids with low σ , collapses of bubbles of a given size are more violent. This is especially interesting if this effect is combined with higher fluid viscosity to establish bubbles which show a similarly violent collapse dynamics as bubbles in water while maintaining larger radii.

Other possibilities for an upscaling of the collapse intensity are the use of lower driving frequencies ω or of larger ambient pressures P_0 at the same P_a/P_0 . These predictions offer a useful guideline to experimenters in search of upscaled single bubble sonoluminescence.

This work has been supported by the DFG under grant SFB 185-D8 and by the joint DAAD/NSF Program for International Scientific Exchange.

Appendix A. Modifications of the RP ODE

As stated in the Introduction, a lot of variations to the RP equation (2.1) are known from literature, see Lastman & Wentzell (1981, 1982) for an overview. We mention here the form derived by Flynn (1975a, 1975b)

$$\begin{aligned} \rho_l \left[\left(1 - \frac{\dot{R}}{c_l} \right) R \ddot{R} + \frac{3}{2} \left(1 - \frac{\dot{R}}{3c_l} \right) \dot{R}^2 \right] &= \left(1 + \frac{\dot{R}}{c_l} \right) \left[p_{gas}(R, t) - P(t) - P_0 - 4\eta_l \frac{\dot{R}}{R} - \frac{2\sigma}{R} \right] \\ &+ \left(1 - \frac{\dot{R}}{c_l} \right) \frac{R}{c_l} \frac{d}{dt} \left[p_{gas}(R, t) - 4\eta_l \frac{\dot{R}}{R} - \frac{2\sigma}{R} \right], \end{aligned} \quad (\text{A } 1)$$

which contains correction terms of higher order in \dot{R}/c_l . It also includes time derivatives of the surface tension and viscosity terms.

Gilmore's equation (see e.g. Hickling 1963) differs from the other RP variations in that its key variable is not pressure, but the enthalpy H of the gas at the bubble wall:

$$\rho_l \left[\left(1 - \frac{\dot{R}}{C_l} \right) R \ddot{R} + \frac{3}{2} \left(1 - \frac{\dot{R}}{3C_l} \right) \dot{R}^2 \right] = \left(1 + \frac{\dot{R}}{C_l} \right) H + \left(1 - \frac{\dot{R}}{C_l} \right) \frac{R}{C_l} \frac{d}{dt} H. \quad (\text{A } 2)$$

Here, the sound speed C_l is not a constant, but depends on H . The exact form of this dependence has to be specified by an equation of state for water, e.g. of modified Tait form (Prosperetti & Lezzi 1986, Cramer 1980). Gilmore's equation was shown in Hickling (1963) to be an accurate description of a collapsing *cavity* up to Mach numbers $|M_l| = |\dot{R}|/C_l$ as high as 5. Its validity for the present problem of collapsing gas bubbles is, however, not well established (Prosperetti 1984).

Figure 2(a) compares the bubble radius dynamics $R(t)$ computed from Eqs. (A 1) and

(A 2) to the solution of (2.1). On this scale, the curves are almost indistinguishable. Only a blow-up of the region around the radius minimum reveals deviations.

As all equations (2.1), (A 1), (A 2) have a common limit for small M_l , significant deviations are only to be expected during collapses, when the bubble wall velocity becomes of order of the sound speed. Figure 2(c) shows M_l for the different $R(t)$ dynamics. Obviously, large differences occur only around the main collapse, and they are not important for the overall dynamics of the bubble, the collapse time interval being exceedingly small. Thus, the RP equation provides a relatively simple and very accurate description of bubble wall motion, which is confirmed by comparison with recent experimental measurements of $R(t)$ in Tian *et al.* (1996). Note also that our criterion (1.1) for energy transfer uses M_g , the Mach number with respect to c_g , which (for argon) is almost 5 times smaller than c_l (in water). Therefore, the energy transfer threshold can be well computed within the RP-SL approach.

Appendix B. Length of afterbounce interval

The Mathieu model equation (4.19) can only be expected to give an accurate description of RP dynamics in the time interval $[\pi/2, 3\pi/2]$, for which it was matched to the Hill equation (4.15) via (4.17). Therefore, we have to compare the afterbounce interval of RP dynamics to this constant interval of length π . Figure 13 shows that for large driving p the Mathieu dynamics gives a good approximation for the end point of the afterbounce interval (starting point of expansion phase), but fails to model the onset time of afterbounces, i.e., the dimensionless collapse time x^* . Thus, the length of the afterbounce interval is smaller than π by a factor of $C(p) = (3\pi/2 - x^*(p))/\pi$.

The collapse time x^* is relatively close to the maximum time x_m . It is therefore convenient to compute it from an expansion of (4.26b) in powers of $(x - \pi/2)$ and $(p - \pi/2)$. This yields

$$x^* \approx 2.55 + 1.72(p - \pi/2) - 1.31(p - \pi/2)^2. \quad (\text{B } 1)$$

The coefficients can be computed analytically, but are of very complicated form. This expression corresponds to a correction factor for the length of the afterbounce interval and, equivalently, for the resonance order k , of

$$C \approx 0.688 - 0.548(p - \pi/2) + 0.418(p - \pi/2)^2. \quad (\text{B } 2)$$

This is the correction introduced in Section 4.3 which is important for a satisfactory description of the resonances of (2.1) by (4.19), see figure 14.

REFERENCES

ABRAMOWITZ, M. & STEGUN, I. A. 1965 *Handbook of Mathematical Functions*. Dover.
 AKHATOV, I. *et al.* 1997, *Phys. Rev. Lett.* **78**, 227.
 ATCHLEY, A. A. 1989, *J. Acoust. Soc. Am.* **85**, 152.
 BARBER, B. P. & PUTTERMAN, S. J. 1991, *Nature* **352**, 318.

BARBER, B. P. & PUTTERMAN, S. J. 1992, *Phys. Rev. Lett.* **69**, 3839.

BARBER, B. P., WENINGER, K., LÖFSTEDT, R. & PUTTERMAN, S. J. 1995, *Phys. Rev. Lett.* **74**, 5276.

BARBER, B. P., WU, C. C., LÖFSTEDT, R., ROBERTS, P. H. & PUTTERMAN, S. J. 1994, *Phys. Rev. Lett.* **72**, 1380.

BERNSTEIN, L. & ZAKIN, M. 1995, *J. Phys. Chem.* **99**, 14619.

BLAKE, F. G. 1949, Harvard University Acoustic Research Laboratory Tech. Memo. **12**, 1.

BRENNER, M. P., HILGENFELDT, S. & LOHSE, D. 1996 Why air bubbles in water glow so easily. In *Nonlinear Physics of Complex Systems – Current Status and Future Trends* (ed. J. Parisi, S. C. Müller, & W. Zimmermann). Lecture Notes in Physics, vol. 476, p. 79. Springer.

BRENNER, M. P., HILGENFELDT, S., LOHSE, D. & ROSALES, R. R. 1996b, *Phys. Rev. Lett.* **77**, 3467.

BRENNER, M. P., LOHSE, D. & DUPONT, T. F. 1995, *Phys. Rev. Lett.* **75**, 954.

BRENNER, M. P., LOHSE, D., OXTOBY, D. & DUPONT, T. F. 1996a, *Phys. Rev. Lett.* **76**, 1158.

BIRKHOFF, G. 1954, *Quart. Appl. Math.* **12**, 306.

CHURCH, C. C. 1988, *J. Acoust. Soc. Am.* **83**, 2210.

CHURCH, C. C. 1989, *J. Acoust. Soc. Am.* **86**, 215.

CRAMER, E. 1980. In *Cavitation and Inhomogeneities in Underwater Acoustics*, p. 54 (ed. W. Lauterborn). Springer.

CRUM, L. A. & CORDRY, S. 1994. In *Bubble dynamics and interface phenomena*, p. 287 (ed. J. Blake *et al.*). Kluwer Academic Publishers.

ELLER, A. & CRUM, L. A. 1970, *J. Acoust. Soc. Am. Suppl.* **47**, 762.

ELLER, A. & FLYNN, H. G. 1964, *J. Acoust. Soc. Am.* **37**, 493.

EVANS, A. K. 1996, *Phys. Rev. E* **54**, 5004.

FLINT, E. B. & SUSLICK, K. S. 1989, *J. Am. Chem. Soc.* **111**, 6987.

FLYNN, H. G. 1975a, *J. Acoust. Soc. Am.* **57**, 1379.

FLYNN, H. G. 1975b, *J. Acoust. Soc. Am.* **58**, 1160.

FROMMHOLD, L. & ATCHLEY, A. A. 1994, *Phys. Rev. Lett.* **74**, 2883.

FYRILLAS, M. M. & SZERI, A. J. 1994, *J. Fluid Mech.* **277**, 381.

GAITAN, D. F. 1990 An experimental investigation of acoustic cavitation in gaseous liquids. Ph.D. thesis, The University of Mississippi.

GAITAN, D. F., CRUM, L. A., ROY, R. A. & CHURCH, C. C. 1992, *J. Acoust. Soc. Am.* **91**, 3166.

GAITAN, D. F. *et al.* 1996, *Phys. Rev. E* **54**, 525.

GOMPF, B. *et al.* 1997, *Phys. Rev. Lett.* **79**, 1405.

HICKLING, R. 1963, *J. Acoust. Soc. Am.* **35**, 967.

HILGENFELDT, S., LOHSE, D. & BRENNER, M. P. 1996, *Phys. Fluids* **8**, 2808.

HILLER, R., PUTTERMAN, S. J. & BARBER, B. P. 1992, *Phys. Rev. Lett.* **69**, 1182.

HILLER, R., WENINGER, K., PUTTERMAN, S. J. & BARBER, B. P. 1994, *Science* **266**, 248.

HINCH, E. J. 1991 Perturbation methods. Cambridge University Press.

HOLT, R. G., GAITAN, D. F., ATCHLEY, A. A. & HOLZFUSS, J. 1994, *Phys. Rev. Lett.* **72**, 1376.

HOLT, R. G. & GAITAN, D. F. 1996, *Phys. Rev. Lett.* **77**, 3791.

KAMATH, V., PROSPERETTI, A. & EGOLFOPOULOS, F. N. 1993, *J. Acoust. Soc. Am.* **94**, 248.

KELLER, J. B. & MIKSIS, M. J. 1980, *J. Acoust. Soc. Am.* **68**, 628.

LAMB, H. 1932 Hydrodynamics. Cambridge University Press.

LASTMAN, G. J. & WENTZELL, R. A. 1981, *J. Acoust. Soc. Am.* **69**, 638.

LASTMAN, G. J. & WENTZELL, R. A. 1982, *J. Acoust. Soc. Am.* **71**, 835.

LAUTERBORN, W. 1976, *J. Acoust. Soc. Am.* **59**, 283.

LIDE, D. R. (ED.) 1991 CRC Handbook of Chemistry and Physics. CRC.

LOHSE, D., BRENNER, M. P., DUPONT, T., HILGENFELDT, S. & JOHNSTON, B. 1997, *Phys. Rev. Lett.* **78**, 1359.

LOHSE, D. AND HILGENFELDT, S. 1997, *J. Chem. Phys.*, **107**, 6986.

LÖFSTEDT, R., BARBER, B. P. & PUTTERMAN, S. J. 1993, *Phys. Fluids A* **5**, 2911.

LÖFSTEDT, R., WENINGER, K., PUTTERMAN, S. J. & BARBER, B. P. 1995, *Phys. Rev. E* **51**, 4400.

MATULA, T. J. *et al.* 1995, *Phys. Rev. Lett.* **75**, 2602.

MATULA, T. J. *et al.* 1997 The acoustic emissions from single-bubble sonoluminescence. Preprint.

MORAN, M. J. *et al.* 1995, *Nucl. Instr. and Meth. in Phys. Res. B* **96**, 651.

MOSS, W. C., CLARKE, D. B., WHITE, J. & YOUNG, D. A. 1994, *Phys. Fluids* **6**, 2979.

MOSS, W. C., CLARKE, D. B. & YOUNG, D. A. 1997, *Science* **276**, 1398.

PLESSET, M. 1949, *J. Appl. Mech.* **16**, 277.

PLESSET, M. 1954, *J. Appl. Phys.* **25**, 96.

PLESSET, M. & PROSPERETTI, A. 1977, *Ann. Rev. Fluid Mech.* **9**, 145.

PROSPERETTI, A. 1977, *Quart. Appl. Math.* **34**, 339.

PROSPERETTI, A. 1984, *Ultrasonics* **22**, 69.

PROSPERETTI, A. & LEZZI, A. 1986, *J. Fluid Mech.* **168**, 457.

RAYLEIGH, LORD 1917, *Philos. Mag.* **34**, 94.

SMEREKA, P., BIRNIR, B. & BANERJEE, S. 1987, *Phys. Fluids* **30**, 3342.

STRUBE, H. W. 1971, *Acustica* **25**, 289.

TIAN, Y., KETTERLING, J. A. & APFEL, R. E. 1996, *J. Acoust. Soc. Am.* **100**, 3976.

VUONG, V. Q. & SZERI, A. J. 1996, *Phys. Fluids* **8**, 2354.

WENINGER, K. R., BARBER, B. P. & PUTTERMAN, S. J. 1997, *Phys. Rev. Lett.* **78**, 1799.

WENINGER, K. R., PUTTERMAN, S. J. & BARBER, B. P. 1996, *Phys. Rev. E* **54**, R2205.

WU, C. C. & ROBERTS, P. H. 1993, *Phys. Rev. Lett.* **70**, 3424.

YASUI, K. 1995, *J. Acoust. Soc. Am.* **98**, 2772.

YOUNG, J. B., SCHMIEDEL, T. & KANG, W. 1996, *Phys. Rev. Lett.* **77**, 4816.